

Research Paper

Linking gold mineralization to regional-scale drivers of mineral systems using in situ U–Pb geochronology and pyrite LA-ICP-MS element mapping

Imogen O.H. Fielding ^{a,*}, Simon P. Johnson ^b, Sebastien Meffre ^c, Jianwei Zi ^{d,e}, Stephen Sheppard ^f, Ross R. Large ^c, Birger Rasmussen ^g



^a Department of Applied Geology, Curtin University, Kent Street, Bentley, WA, 6102, Australia

^b Geological Survey of Western Australia, 100 Plain Street, East Perth, WA, 6004, Australia

^c CODES ARC Centre of Excellence in Ore Deposits, University of Tasmania, Private Bag 126, Hobart, TAS, 7001, Australia

^d State Key Lab of Geological Processes and Mineral Resources, China University of Geosciences, Wuhan 430074, China

^e John de Laeter Centre, Curtin University, Kent Street, Bentley, WA, 6102, Australia

^f Calidus Resources Ltd, Suite 12, 11 Ventnor Avenue, West Perth, WA, 6005, Australia

^g School of Earth Sciences, The University of Western Australia, Perth, WA, 6009, Australia

ARTICLE INFO

Article history:

Received 13 March 2018

Received in revised form

24 April 2018

Accepted 17 June 2018

Available online 24 July 2018

Keywords:

Geochronology

Xenotime

SHRIMP

LA-ICP-MS

Gold mineralization

Capricorn orogen

ABSTRACT

Proterozoic orogens commonly host a range of hydrothermal ores that form in diverse tectonic settings at different times. However, the link between mineralization and the regional-scale tectonothermal evolution of orogens is usually not well understood, especially in areas subject to multiple hydrothermal events. Regional-scale drivers for mineral systems vary between the different classes of hydrothermal ore, but all involve an energy source and a fluid pathway to focus mineralizing fluids into the upper crust. The Mount Olympus gold deposit in the Proterozoic Capricorn Orogen of Western Australia, was regarded as an orogenic gold deposit that formed at ca. 1738 Ma during the assembly of Proterozoic Australia. However, the trace element chemistry of the pyrite crystals closely resembles those of the Carlin deposits of Nevada, with rims that display solid solution gold accompanied by elevated As, Cu, Sb, Hg, and Tl, surrounding gold-poor cores. New SHRIMP U–Pb dating of xenotime intergrown with auriferous pyrite and ore-stage alteration minerals provided a weighted mean $^{207}\text{Pb}^*/^{206}\text{Pb}^*$ date of 1769 ± 5 Ma, interpreted as the age of gold mineralization. This was followed by two discrete episodes of hydrothermal alteration at 1727 ± 7 Ma and 1673 ± 8 Ma. The three ages are linked to multiple reactivation of the crustal-scale Nanjilgardy Fault during repeated episodes of intracratonic reworking. The regional-scale drivers for Carlin-like gold mineralization at Mount Olympus are related to a change in tectonic regime during the final stages of the intracratonic 1820–1770 Ma Capricorn Orogeny. Our results suggest that substantial sized Carlin-like gold deposits can form in an intracratonic setting during regional-scale crustal reworking.

© 2018, China University of Geosciences (Beijing) and Peking University. Production and hosting by Elsevier B.V. This is an open access article under the CC BY-NC-ND license (<http://creativecommons.org/licenses/by-nc-nd/4.0/>).

1. Introduction

The mineral systems concept describes how an ore deposit is the expression of a number of processes operating at a range of spatial and temporal scales (Wyborn et al., 1994; McCuaig and Hronsky, 2014; Huston et al., 2016). At the largest scale, mineralization is driven by a regional energy source with the transport of

hydrothermal fluids or magmas along crustal-scale pathways (McCuaig and Hronsky, 2014; Huston et al., 2016). Whereas the smallest scale relates to local variations within an individual prospect or deposit, such as alteration mineralogy, element association, and the type of host rocks to mineralization (Robert et al., 2007). The absolute age of mineralization and its timing relative to regional-scale tectonothermal events, is often poorly known but is critical for understanding the causes of ore formation (Hronsky et al., 2012). Without this information the key factors in ore generation may not be correctly identified, particularly in areas that have been subject to multiple hydrothermal or crustal reworking events (e.g. Rasmussen et al., 2006).

* Corresponding author.

E-mail address: imogen.fielding@postgrad.curtin.edu.au (I.O.H. Fielding).

Peer-review under responsibility of China University of Geosciences (Beijing).

The drivers for orogenic and epithermal gold mineralization are relatively obvious. Orogenic deposits are associated with active margins undergoing compressional tectonic activity during accretionary or collisional orogenic events (Groves et al., 1998; Goldfarb et al., 2001), and epithermal deposits are intimately associated with coeval magmatism (e.g. Simmons et al., 2005). However, the drivers for Carlin-type deposits (Cline et al., 2005) are more enigmatic because such deposits do not always have a clear link between regional-scale tectonomagmatic activity and crustal architecture (e.g. Hu et al., 2002; Cline et al., 2005; Muntean et al., 2011).

The Mount Olympus gold deposit is located in the northern Capricorn Orogen within the West Australian Craton (Fig. 1). The area has been subjected to limited research with few peer reviewed publications (e.g. Sener et al., 2005; Wells et al., 2016), and the most comprehensive ore-body descriptions are sourced from conference abstracts and open-file company reports (e.g. Morant and Doepel, 1997; Young et al., 2003). Mount Olympus has many of the characteristics of a Carlin-type deposit including strata-bound ore, invisible gold concentrated in arsenian pyrite, and ore-stage alteration assemblages characterized by quartz, illite and sericite with the removal of carbonate minerals (Young et al., 2003). Despite these similarities, Sener et al. (2005) linked xenotime growth (and gold deposition) at ca. 1738 Ma to orogenic events related to the assembly of Proterozoic Australia. However, there are no orogenic events known in Western Australia at ca. 1738 Ma, which falls between the 1820–1770 Ma Capricorn Orogeny and the 1680–1620 Ma Mangaroon Orogeny, both of which represent periods of intracratonic reworking that resulted in deformation, metamorphism and granite intrusion inboard of the plate margin (Sheppard et al., 2005, 2010).

This study has two aims: (1) to review the classification of gold mineralization at Mount Olympus by assessing both the macroscopic characteristics and the distribution of trace element in pyrite crystals, and making comparisons to documented Carlin-type and orogenic gold deposits (e.g. Large et al., 2009); and (2) to present

new in situ U-Pb xenotime geochronological data obtained using the Sensitive High Resolution Ion Microprobe (SHRIMP) to determine the timing of hydrothermal events, including gold mineralization. These data are then integrated with the record of the well-established crustal architecture and tectonothermal events in the West Australian Craton (Johnson et al., 2013) to investigate the large-scale mineral system processes associated with the Mount Olympus deposit.

2. Geological background

The Capricorn Orogen is a zone of variably deformed rocks between the Pilbara and Yilgarn cratons of Western Australia (Fig. 1; Tyler and Thorne, 1990). The orogen records the two-stage assembly of the West Australian Craton by ca. 1950 Ma (Johnson et al., 2011), as well as at least five younger episodes of intracratonic reworking spanning over a billion years (Sheppard et al., 2005, 2007; Johnson et al., 2017; Korhonen et al., 2017). In the northern part of the Capricorn Orogen, Paleoproterozoic siliciclastic, carbonate and volcanic rocks of the Wyloo and Shingle Creek Groups were deformed during the 1820–1770 Ma Capricorn Orogeny (Thorne and Seymour, 1991). Mineralization throughout the region has a spatial association with crustal-scale faults (Johnson et al., 2013). The Nanjilgardy Fault (Fig. 1), in particular, has experienced multiple reactivations that led to deposition and remobilization of various styles of gold mineralization throughout the northern Capricorn Orogen (Johnson et al., 2013; Fielding et al., 2017).

3. Deposit description

The Mount Olympus gold deposit has a total remaining resource of 15 million tonnes (Mt) at 2.2 g/t containing ~1 Moz of gold (Northern Star Resources Limited, 2015). Mineralization occurs where the Zoe Fault, a second order splay of the Nanjilgardy Fault,

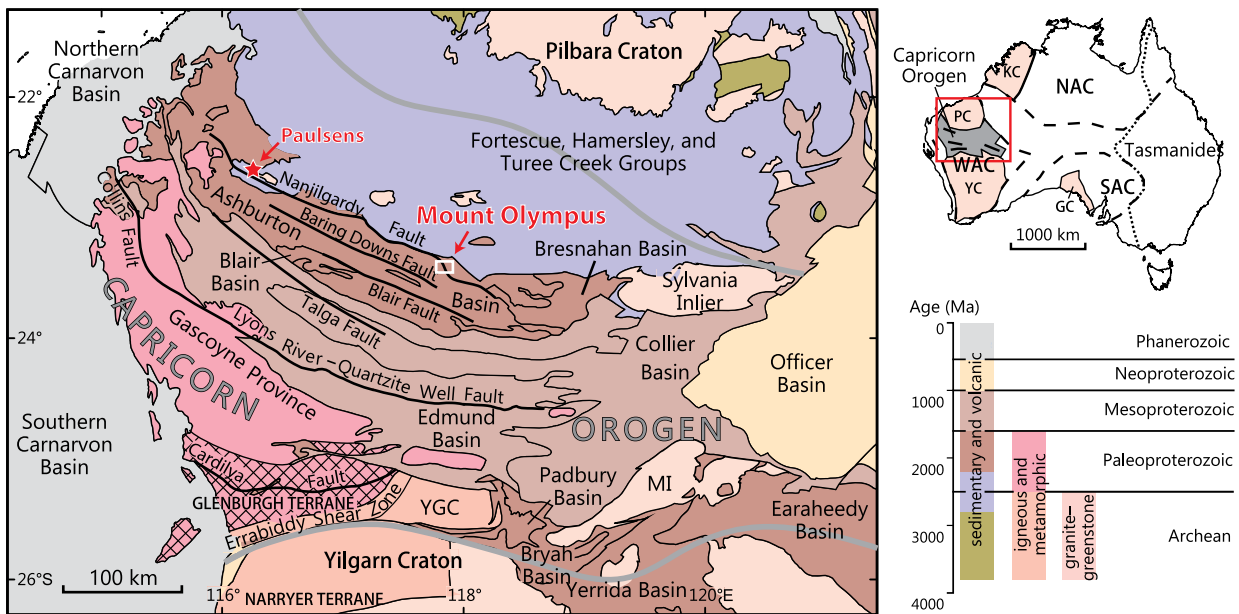


Figure 1. Regional geology of the northern Capricorn Orogen showing the location of Mount Olympus and Paulsens gold mines. White box indicates the inset map shown in Fig. 2A. Abbreviations: GC = Gawler Craton, KC = Kimberley Craton, MI = Marymia Inlier, NAC = North Australian Craton, PC = Pilbara Craton, SAC = South Australian Craton, WAC = West Australian Craton, YC = Yilgarn Craton, YGC = Yarlarweelor Gneiss Complex (after Johnson et al., 2013).

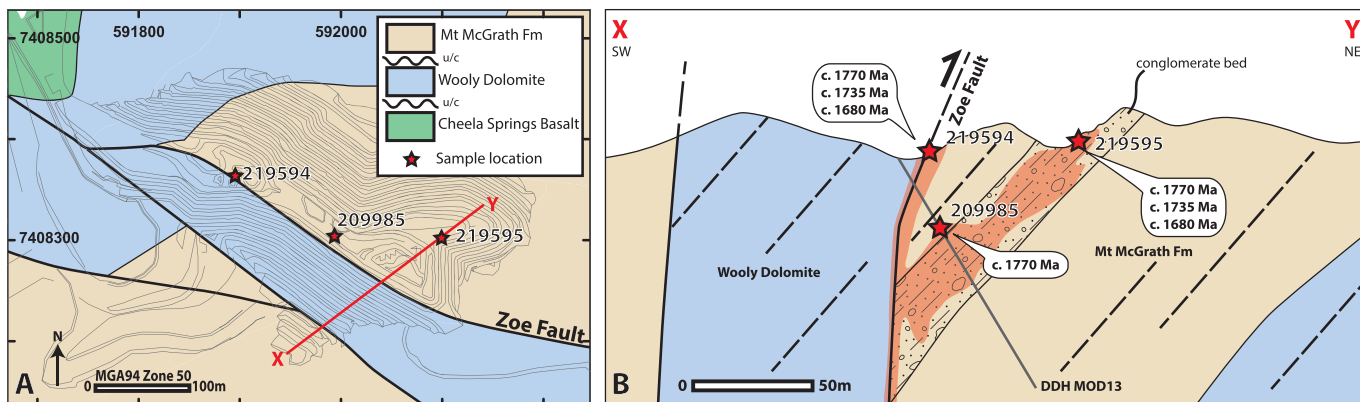


Figure 2. (A) Prospect scale geological map of the Mount Olympus pit showing geochronology sample locations. (B) Schematic cross section of the Mount Olympus ore body with geochronology sample locations.

juxtaposes conglomerate and coarse-grained sandstone of the Mount McGrath Formation against dolomitic mudstone of the Wooly Dolomite (Fig. 2; Morant and Doepl, 1997; Krapez et al., 2015). The Zoe Fault is a dextral transpressional fault which has a strong control on the location of gold mineralization and is likely to have been the primary conduit for mineralizing fluids (Young et al., 2003).

Two distinct types of mineralized lodes are evident in the Mount Olympus pit: (1) strata-bound ore where arsenian pyrite crystals up to 1 cm in diameter are disseminated within carbonaceous and ferruginous conglomerate and sandstone of the Mount McGrath Formation, and (2) fault-hosted mineralization is associated with pyrite and graphite, or in rare instances is associated with strongly deformed quartz veins and stringers along the Zoe Fault (Fig. 2B; Morant and Doepl, 1997; Young et al., 2003). In both lodes, gold forms microscopic inclusions in pyrite or as a solid solution within visibly zoned arsenian pyrite (Young et al., 2003). Ore-stage alteration assemblages are reported to have formed at up to 350 °C at 1–2 kbar (Young et al., 2003) and include quartz, muscovite, kaolin-group phases (kaolinite and dickite) and pyrophyllite, with the removal of chlorite and carbonate minerals (Wells et al., 2016).

4. Methods

4.1. LA-ICP-MS

Pyrite from within mineralized zones of the Mount Olympus deposit were collected from diamond drill cores MOD13 and NMOD002 (Table 1) for analysis by LA-ICP-MS. Polished 25 mm diameter rock mounts were prepared and pyrites were etched using a dilute nitric acid solution to reveal any internal growth zones in order to select areas suitable for trace element mapping by LA-ICP-MS. Trace element mapping of pyrite crystals were performed at the ARC Centre of Excellence in Ore Deposits LA-ICP-MS facility at

the University of Tasmania using the New Wave 213-nm solid-state laser microprobe coupled to an Agilent 4500 quadrupole ICP-MS. The procedure outlined in Large et al. (2009) was followed and described briefly below.

Trace element distribution maps were generated by ablating parallel lines in a grid pattern. Beam sizes of 15, 22, 35 and 47 µm were used with a laser beam repetition rate of 10 Hz with energy maintained at 4.5 J/cm². Rastering speed for each line was equal to the beam size per second (i.e., 15–47 µm/s). Analysis consisted of 28 elements including Na, Mg, Al, Si, K, Ca, Ti, V, Mn, Fe, Co, Ni, Cu, Zn, As, Se, Mo, Ag, Sb, Te, W, Pt, Au, Hg, Ti, Pb, Bi and U. Acquisition time was set to 0.03 s for gold, 0.008 s for chalcophile elements, and 0.002 s for other elements resulting in a total quadrupole sweep time of 0.2 s (including deadtime).

Data were collected in counts per second (cps) and later converted to parts per million (ppm). The conversion was undertaken using the in-house standard STDGL2b-2, analyzed both before and after each sample with a 74 µm spot size, laser beam repetition rate of 10 Hz and energy of 4 J/cm². The standard comprises a homogenous mix of powdered sulfide and trace elements of known concentrations, fused into a lithium borate glass disk (Danyushevsky et al., 2011). Instrumental mass bias was initially determined using standard laser ablation data reduction techniques then applied to each quadrupole sweep (i.e., each pixel in the image) assuming stoichiometric Fe (456,000 ppm) in pyrite for each line of the image. The data are expected to be accurate for the pyrite in each image, but will tend to underestimate the concentrations for other mineral phases due to the different behavior of other minerals during ablation relative to pyrite (matrix effects). The ratios between elements will not be affected by these problems. Hg was not quantified due to the lack of standards and the volatility of the element. The Hg counts per second images can be used on a qualitative basis to identify high and low Hg zones.

Table 1
LA-ICP-MS sample location, descriptions and gold grades.

Hole ID	MGA94 zone 50		Depth (m)	Description	Whole rock Au assay from diamond core
	East	North			
NMOD002	592408	7407945	377.7	Semi-massive pyrite in silicified black shale	4.86 ppm (377–378 m)
NMOD002	592408	7407945	376.2	Semi-massive pyrite in silicified black shale	3.58 ppm (376–377 m)
MOD13	591962	7408248	130.6	Sericite altered sandstone with coarse euhedral pyrite and arsenopyrite	1.92 ppm (130–131 m)
MTO90	592159	7408094	262.3	Sericite altered siltstone with coarse euhedral pyrite	0.92 ppm (262–263 m)

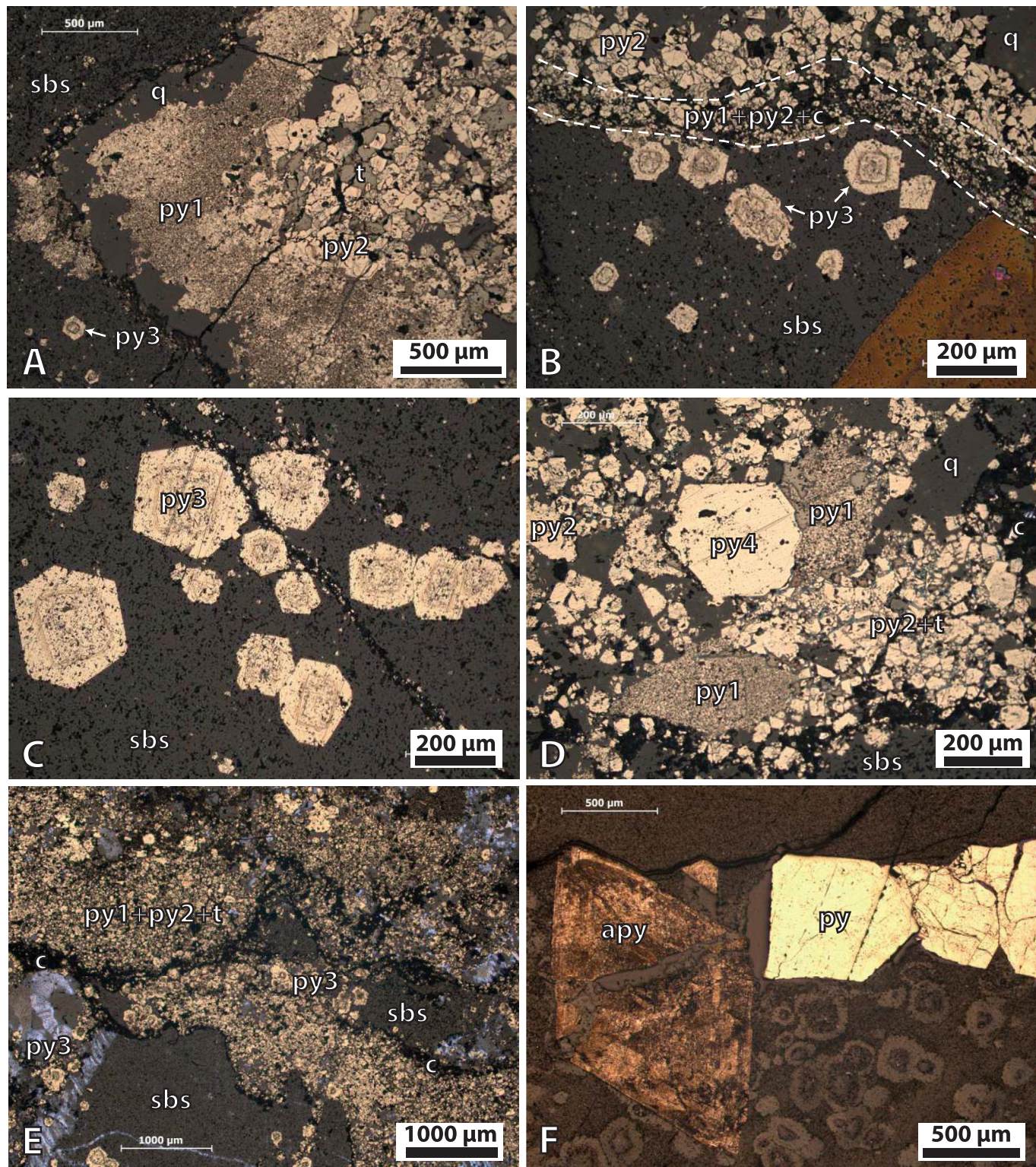


Figure 3. Textures of pyrite types at the Mount Olympus deposit. (A) NMOD002 377.7 m in depth showing py1 surrounding py2 and tetrahedrite. (B) NMOD002 377.7 m in depth showing a narrow band of py1, py2 and carbonaceous material separating py2 from py3. (C) NMOD002 376.2 m in depth growth zoning in py3. (D) NMOD002 376.2 m depth py1, py2 and large euhedral py4. (E) Py1, py2 and tetrahedrite separated from py3 by a carbonaceous rich band and silicified black shale. (F) MOD13 130.6 m in depth, showing large pyrite and arsenopyrite crystals from the strata-bound mineralization. Abbreviations: py—pyrite, t—tetrahedrite, sbs—silicified black shale, q—quartz, c—carbonaceous material, apy—arsenopyrite.

4.2. Geochronology

Three mineralized samples were examined by optical and scanning electron microscope to identify xenotime suitable for geochronology. Small disks of thin section containing xenotime crystals for SHRIMP analysis were drilled out of the polished thin-sections before being cast into 25 mm epoxy SHRIMP mounts. Xenotime standards MG1, Xeno1 and Xeno2 were placed on a separate SHRIMP mount that was gold coated along with the sample mounts. SHRIMP U–Pb dating of xenotime followed established procedures for small-spot, in situ analysis as outlined by Fletcher et al. (2000, 2004).

A primary beam of O^{2−} ions was focused through a 30 μm Kohler aperture to produce an oval 10–15 μm wide spot on the sample surface with a current of 0.2–0.8 nA. The secondary ion system was focused through a 100 μm collector slit onto an electron multiplier to produce mass peaks with flat tops and a mass resolution of >5200 in all sessions. Background counts from scattered ions were reduced using a flight retardation lens, which is known to cause slight session-dependent instrumental mass fractionation (IMF) of Pb isotopes. IMF corrections were applied to all analyses.

Data were collected in sets of 8 scans, with xenotime reference materials analyzed every 4–6 sample analyses. Count times per scan for background position 204.045, and Pb isotopes 204, 206, 207, and 208 were 10, 10, 10, 30 and 10 s, respectively. Xenotime was analyzed with a 9-peak run table following analytical protocols detailed by Fletcher et al. (2004). Pb/U calibrations and matrix corrections for U and Th contents were based on concurrent measurements of the standards MG-1 (Fletcher et al., 2004) and z6413 ("Xeno1"; Stern and Rayner, 2003). Pb/Th was determined indirectly, using a fixed Th/U calibration (Fletcher et al., 2004). Matrix corrections for REE assumed the samples have REE abundances similar to Xeno1.

Raw data from analyses were processed using the SQUID 2 add-in (v. 2.50.12.03.08) for Excel 2003 (Ludwig, 2009), and plotted using the ISOPLOT add-in (v. 3.76.12.02.24; Ludwig, 2003). Common-Pb corrections were based on measured ²⁰⁴Pb/²⁰⁶Pb ratios and contemporaneous Pb composition according to the terrestrial Pb evolution model of Stacey and Kramers (1975). Matrix effect corrections were made for all xenotime data using procedures described by Fletcher et al. (2004). Pooled ages are quoted with 95% confidence levels, whereas individual analyses are presented with 1σ errors.

5. Results

5.1. LA-ICP-MS

The content and distribution of trace elements within massive pyrite from gold-rich samples differs between those in

carbonaceous-rich material from the Zoe Fault (NMOD002), and those within sericite-altered sandstone (MOD13) from strata-bound mineralization.

5.1.1. Zoe Fault

Polished 25 mm diameter rock mounts were prepared of massive pyrite-bearing black shale from the Zoe Fault in drill core NMOD002 at 377.7 m and 376.2 m to investigate the textures and internal trace element zoning within the pyrite. These samples are from a zone of high-grade mineralization containing whole-rock gold assay results of 3.58 ppm (376–377 m) and 4.86 ppm (377–378 m). Two areas of pyrite from the thin sections at 377.7 m and two at 376.2 m, were mapped in detail by LA-ICP-MS.

Four types of pyrite have been defined in samples from NMOD002 (Fig. 3A–E) with a paragenetic sequence from pyrite 1 (py1) to pyrite 4 (py4) summarized in Table 2. Py1 comprises micro-crystal aggregates (Fig. 3A, D) which often form in carbon-rich horizons (Fig. 3B). Py2 is composed of coarse-grained, subhedral pyrite that is commonly intergrown with tetrahedrite (Fig. 3A, B, D), or along carbonaceous layers (Fig. 3B). Py3 forms within the silicified shale matrix as euhedral crystals with internal zoning that shows a change from the cubic to pyritohedral crystal form from the internal zone to the rim (Fig. 3B and C). Py4 is a coarse, inclusion-free pyrite up to 300 μm across (Fig. 3D).

Trace element images of each type of pyrite show that py1 has a mean Au grade of 8 ppm and is also enriched in As, Tl ± Pb (Figs. 4 and 5). Py2 is low in both Au and As (Fig. 6), with a mean Au content of 2 ppm and is often intergrown with tetrahedrite which is enriched in Cu, Zn, Ag, Sb, Hg (Figs. 4 and 5). Py3 is zoned with an internal growth band enriched in Au (Figs. 6 and 7) and has the highest gold values (up to 429 ppm) of all samples analyzed. The core zone contains minor Hg, Pb and Bi with a mean Au content of 5 ppm, the internal zone has elevated Au, As, Cu, Hg, Tl and Sb and a mean Au content of 67 ppm, and the rim zone is Co and Ni rich and has a gold content of 4 ppm (Fig. 7). The interface zone between areas with abundant py1, py2 and tetrahedrite against areas of silicified black shale containing py3 is commonly defined by a band of carbonaceous material (Fig. 3B, E) enriched in Au, Mo, V, U and Al (Fig. 6). Py4 has low trace elements concentrations and does not contain any gold (Fig. 5).

5.1.2. Strata-bound mineralization

Polished mounts were prepared from a sericite-altered sandstone with a whole rock gold assay of 1.92 ppm (130–131 m) collected from diamond drill core MOD13 at 130.6 m (Fig. 3F). The sample contains abundant, coarse, euhedral pyrite and arsenopyrite crystals. The pyrite has a thick (100–300 μm) diffusive rim zone with a mean Au value of 55 ppm. This surrounds a core with lower values of both As and Au (mean 12 ppm Au). These pyrites have no other trace element associations (Fig. 8).

Table 2
Summary of paragenetic sequence from py1 to py4.

Drill hole	Paragenesis	Lode	Description	Trace element association
NMOD002	Py1	Zoe Fault	Micro-crystals aggregates; formed in carbon band commonly with py2 and tetrahedrite	Au 7.78 ppm, As, Tl + Pb
NMOD002	Py2	Zoe Fault	Coarse grained subhedral pyrite; commonly intergrown with tetrahedrite; occurs with py1 in carbon rich bands	Low levels of Au (1.85 ppm) and As
NMOD002	Py3	Zoe Fault	Euhedral pyrite with internal zonation; internal band is cubic, rim is pyrohedral	Core: Au 4.85 ppm; Hg-Pb-Bi Internal band: Au 67.28 ppm; Au-As-Cu-Hg-Tl-Sb Rim: Au 3.56 ppm; Co-Ni
NMOD002 MOD13	Py4 Tetrahedrite	Zoe Fault Strata-bound	Coarse (>300 μm) clear pyrite Coarse grained and intergrown with py2 Coarse euhedral pyrite and arsenopyrite; thick (100–300 μm) diffusive rim zone	No Au; depleted in trace elements Cu-Zn-Ag-Sb-Hg Au 55.06 ppm; As enriched

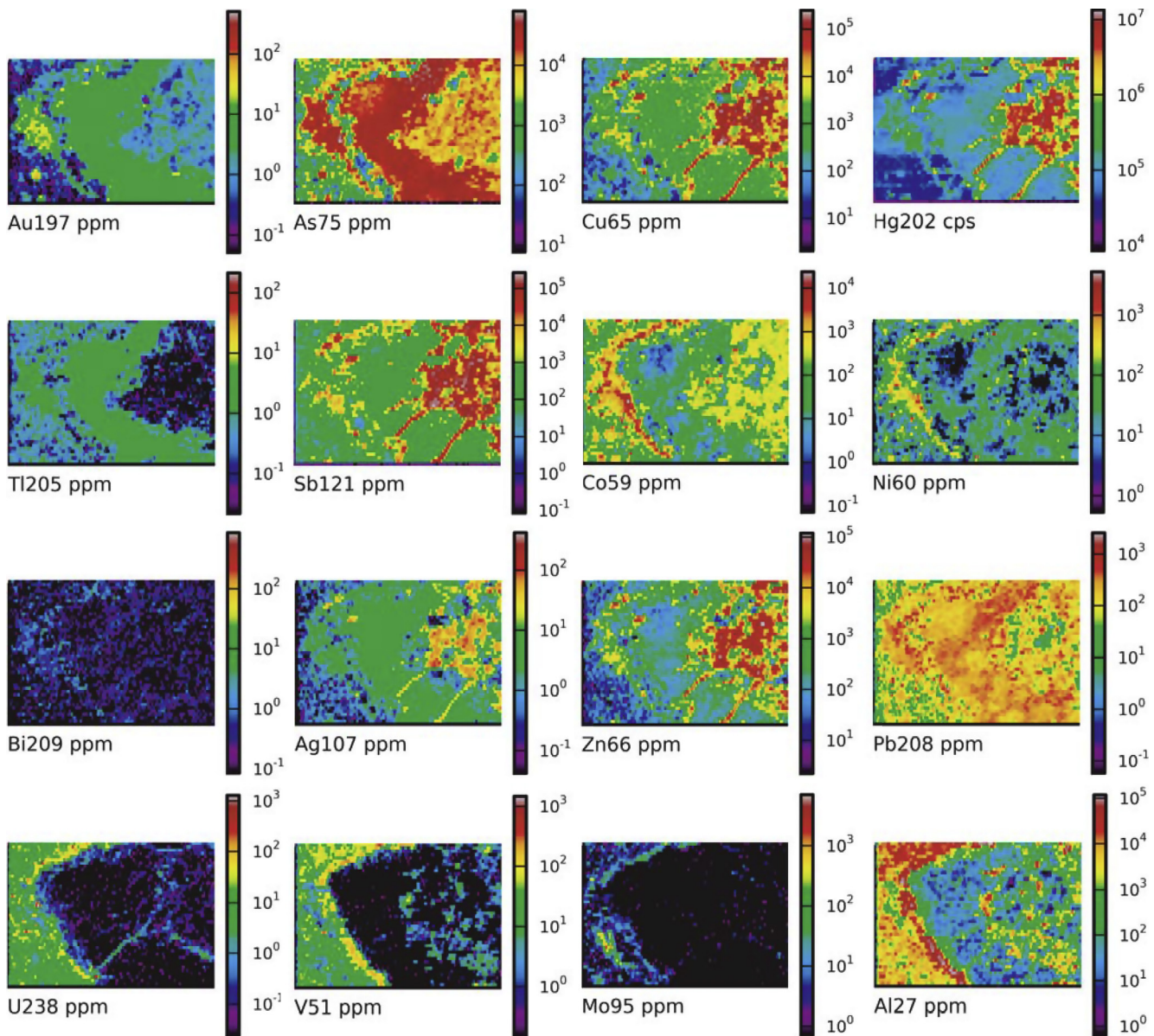


Figure 4. LA-ICP-MS images of trace elements in pyrite from NMOD002 377.7 m depth showing py2 and tetrahedrite surrounded by a py1 (refer to Fig. 3A). Py1 is associated with elevated Au, As, Ti and Pb, py2 is slightly enriched in Au and As and tetrahedrite is enriched in Cu, Hg, Sb, Ag and Zn.

6. Geochronology

6.1. GSWA 219594: Zoe Fault mineralization

A mineralized sample from the Zoe Fault (MGA 94 Zone 50 591903E, 7408364N) comprising brecciated pyrite (py1–4), carbonaceous material and quartz veins, contained small xenotime crystals (<20 µm diameter) in the brecciated parts of the sample. The xenotime commonly forms overgrowths on zircon crystals (Fig. 9A) and contains inclusions of quartz, muscovite and rutile.

Twenty-six analyses were conducted on 20 xenotime crystals with U contents ranging from 1053 ppm to 4638 ppm and Th contents between 392 ppm and 8441 ppm. Three analyses >10% discordant and two analyses with imprecise data due to poor spot placement were excluded from the age determination. The remaining 21 analyses yielded three distinct age modes (Fig. 10A, Table 3) with weighted mean $^{207}\text{Pb}*/^{206}\text{Pb}^*$ dates of 1768 ± 8 Ma

(MSWD = 1.12, $n = 9$), 1727 ± 8 Ma (MSWD = 1.08, $n = 10$) and 1671 ± 18 Ma (MSWD = 0.15, $n = 2$). No textural differences between the xenotime grains within each of these age modes could be identified.

6.2. GSWA 209985: strata-bound mineralization

A sample of strata-bound mineralization (drill hole MOD13, depth 91.23–91.25 m, MGA 94 Zone 50 591962E, 7408248N) was taken from a pervasively altered siltstone with coarse pyrite and 2.67 ppm of Au, similar to the sample analyzed by LA-ICP-MS for trace element analyses. Small xenotime (<25 µm diameter) crystals intergrown with ore-related alteration minerals, quartz and muscovite (Fig. 9B), and some grains are fully contained within pyrite crystals (Fig. 9C).

Twenty analyses conducted on 20 xenotime crystals with U and Th contents ranging from 1118 ppm to 4190 ppm and 57,274 ppm to

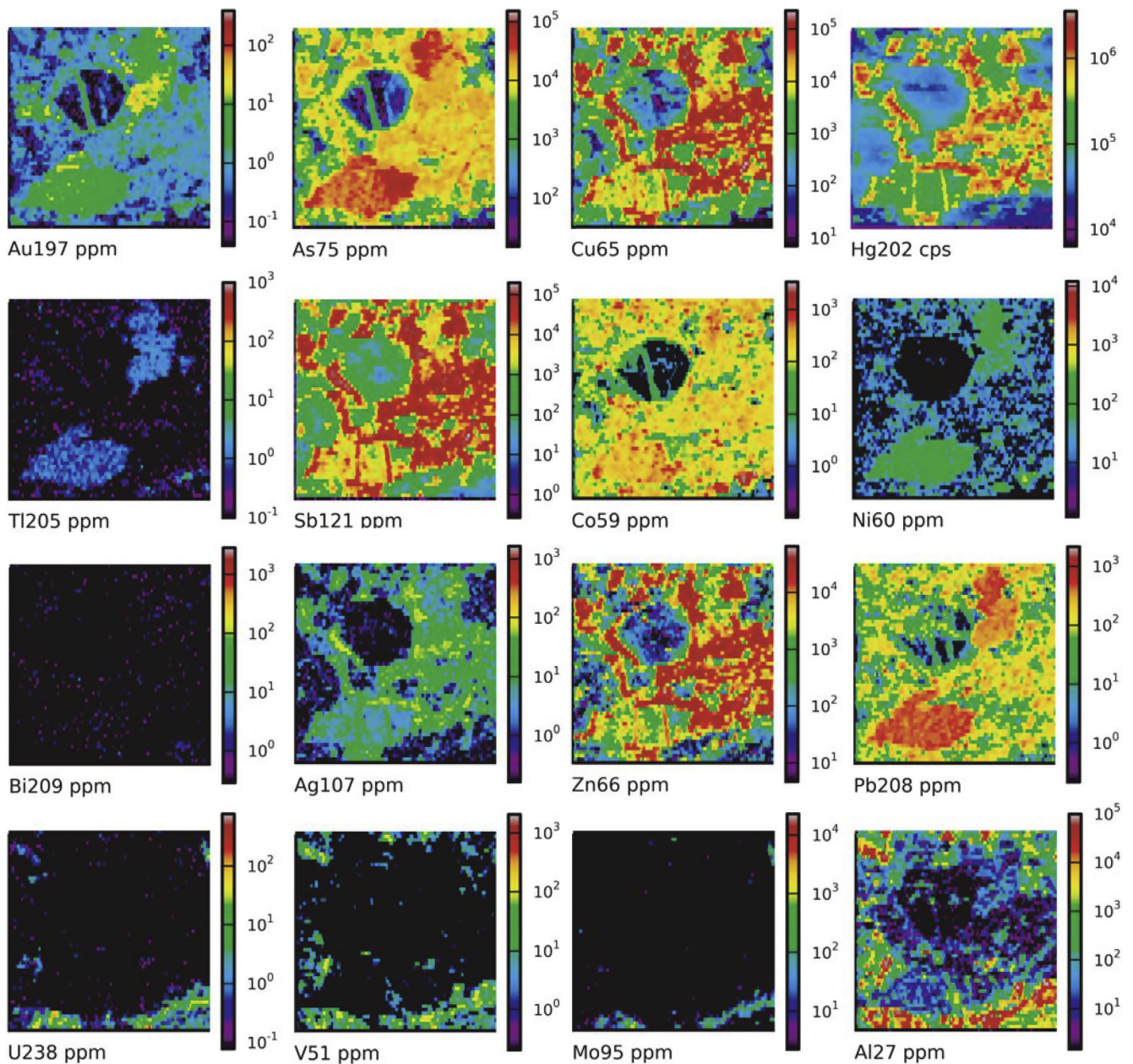


Figure 5. LA-ICP-MS images of trace elements in pyrite from NMOD002 376.2 m in depth (refer to Fig. 3D) showing py4 with no trace element associations. Py1 is enriched in Au, As, Ti, Pb, and py2 and tellurium are intergrown and enriched in Au, As, Cu, Hg, Sb, Ag and Zn.

21,590 ppm, respectively. Three of the analyses were excluded from the age determination due to >10% discordance. The remaining 17 analyses yielded a weighted mean $^{207}\text{Pb}^*/^{206}\text{Pb}^*$ date of 1770 ± 7 Ma (MSWD = 1.4; Fig. 10B, Table 4). This sample, which contains 2.67 ppm Au, is the only one in which xenotime is encased in auriferous pyrite and provides a unimodal age. Together these data suggest that the date obtained represents the timing of hydrothermal alteration associated with pyrite crystallization and gold mineralization.

6.3. GSWA 219595 strata-bound mineralization

A second sample of strata-bound mineralization (MGA 94 Zone 50 592095E, 7408303N) was collected from quartz–muscovite–

altered conglomerate in the Mount Olympus pit with pyrite crystals up to 2 cm. Xenotime crystals from this sample are up to 80 μm in diameter and commonly contain inclusions of quartz, zircon, rutile or muscovite (Fig. 9D).

Twenty-eight analyses were obtained on 20 xenotime crystals with U contents between 514 and 4338 ppm and Th contents from 1124 to 7288 ppm. Two analyses with >10% discordance and two analyses with imprecise data due to poor spot placement were excluded from the age determination. The remaining 24 analyses yielded three distinct age modes (Fig. 10C, Table 5) with weighted mean $^{207}\text{Pb}^*/^{206}\text{Pb}^*$ dates of 1764 ± 11 Ma (MSWD = 0.04, $n = 7$), 1727 ± 13 Ma (MSWD = 0.57, $n = 9$) and 1674 ± 12 Ma (MSWD = 1.4, $n = 8$). No textural differences between the xenotime grains within each of these age modes could be identified.

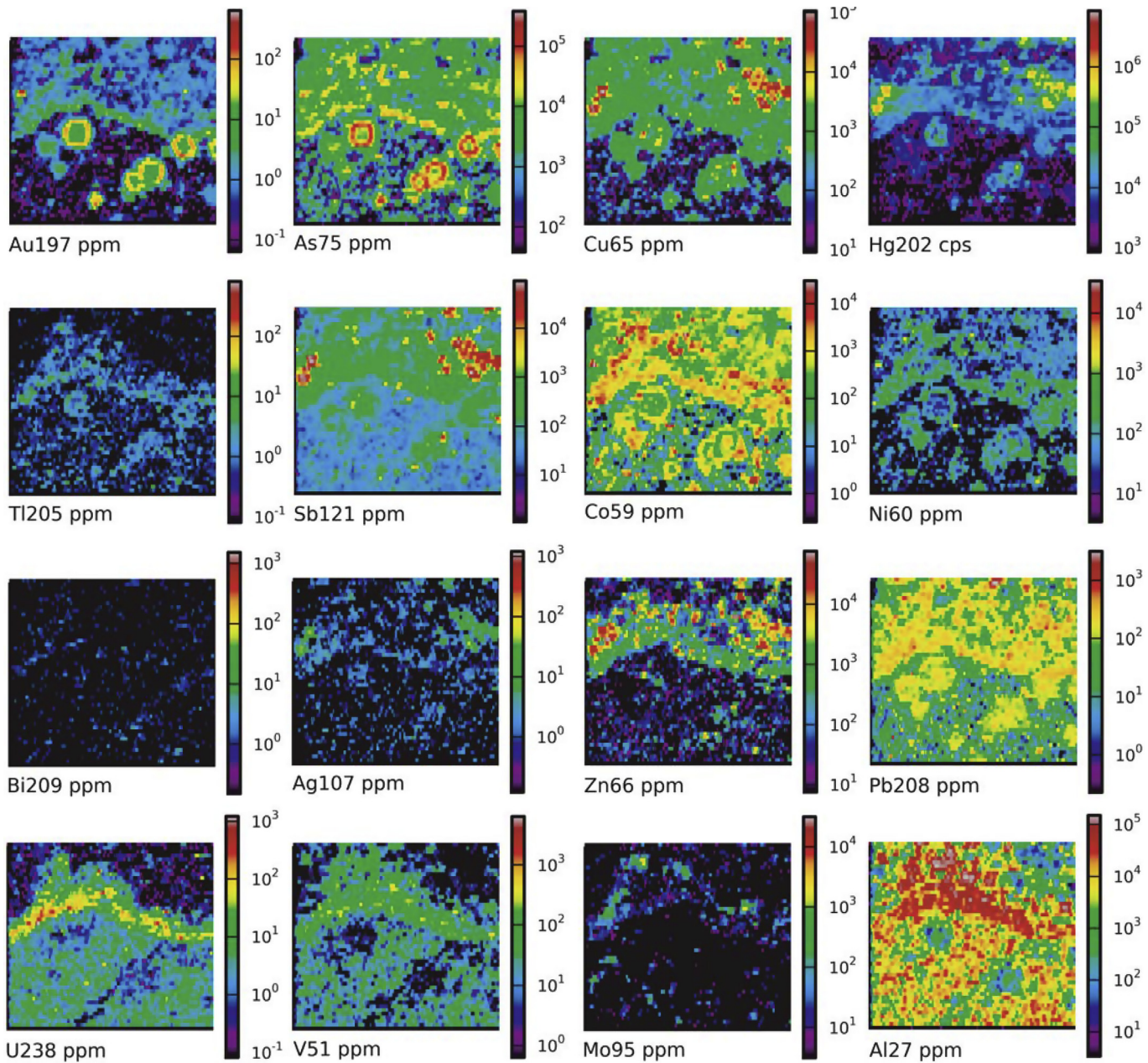


Figure 6. LA-ICP-MS image of trace element from pyrite in NMOD002 377.7 m depth showing a narrow band of py1, py2 and carbonaceous material separating py2 from py3 (refer to Fig. 3B). The carbonaceous band is enriched in Au, U, V, Mo and Al.

6.4. Pooled age data

The distinct age modes obtained from all three samples are consistent (Fig. 11) thus allowing the pooling of all data to better define the age peaks. Pooled data yield weighted mean $^{207}\text{Pb}^*/^{206}\text{Pb}^*$ dates of 1769 ± 4 Ma (MSWD = 1.02, $n = 33$), 1727 ± 7 Ma (MSWD = 0.79, $n = 19$) and 1673 ± 8 Ma (MSWD = 1.15, $n = 10$). The ca. 1730 Ma and 1675 Ma ages are interpreted to represent discrete hydrothermal events causing new growth or dissolution and re-precipitation of xenotime, whereas the ca. 1770 Ma age, which is common to all studied samples, represents the timing of pyrite crystallization and gold mineralization. These new geochronological data indicate a more complex geological history of the Mount Olympus deposit than previously recognized by Şener et al. (2005).

7. Discussion

7.1. Deposit classification

The classification of the Mount Olympus deposit has been reported as having features similar to both Carlin-type and orogenic gold deposits (Young et al., 2003; Şener et al., 2005); however, these styles of mineralization are significantly different (Table 6). Orogenic gold deposits are generally related to accretionary or collisional events where gold deposits occur as linear trends associated with trans-crustal structures that mark suture zones between continental blocks (Groves et al., 1998; Goldfarb et al., 2001; Hronsky et al., 2012). Deposits are hosted by Archean greenstones or Paleoproterozoic and Phanerozoic turbidite deposits that are metamorphosed to greenschist facies (Goldfarb and Groves, 2015). Commonly the

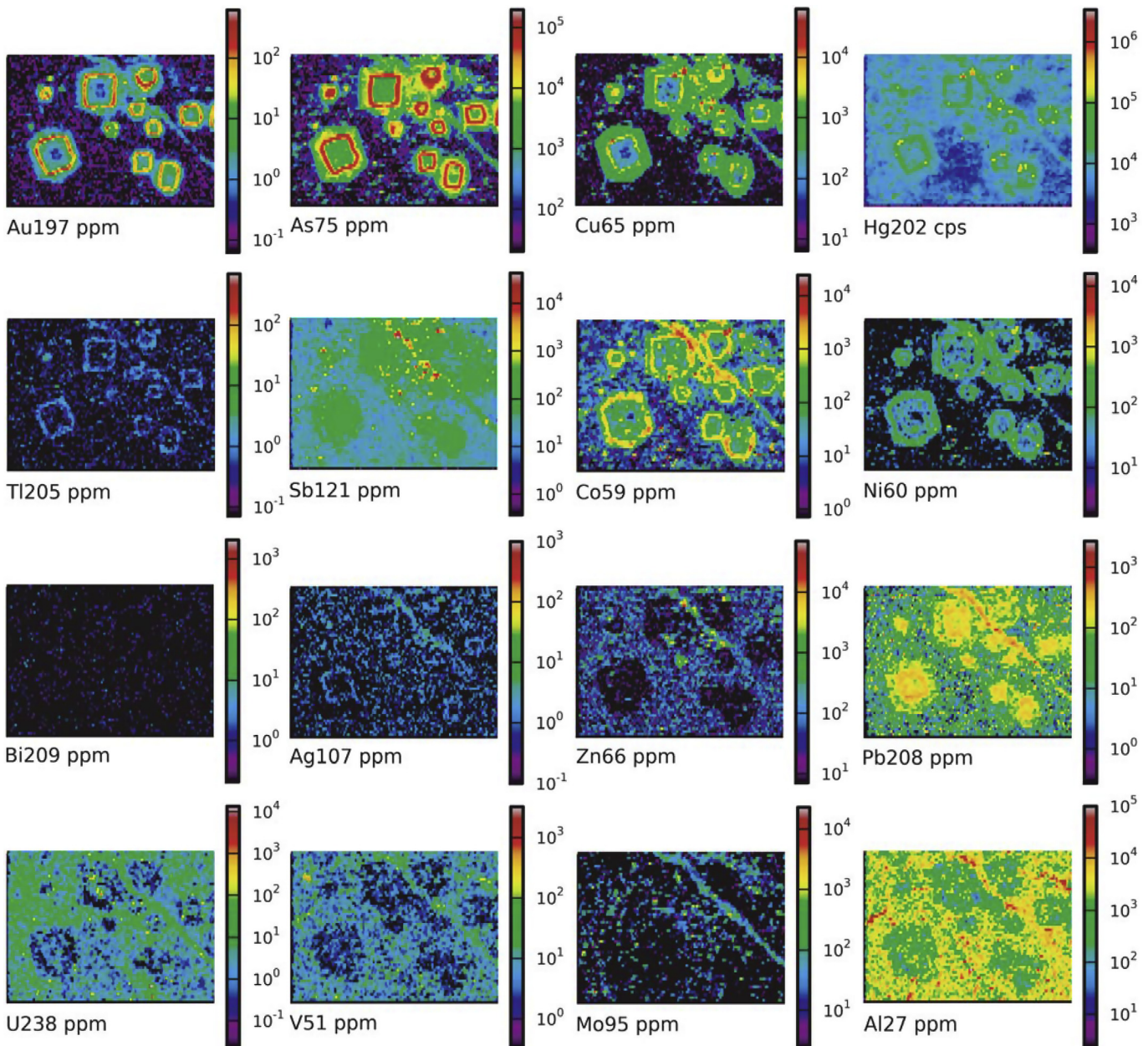


Figure 7. LA-ICP-MS image of trace elements from pyrite in NMOD002 376.2 m depth showing zoning in py3 (see Fig. 3C) with an core enriched in As, Hg, Sb and Pb, an internal band enriched in Au, As, Cu, Hg, Ti, Sb and Pb, and a rim zone associated with elevated Co and Ni.

deposits have ore-stage alteration assemblages of carbonate-iron sulfide \pm white mica \pm chlorite that formed at 200–650 °C and 0.5–5 kbar (Goldfarb et al., 2001; Groves et al., 2003) in which mineralization is associated with quartz \pm carbonate-sulfide veins (Groves et al., 1998). Trace element compositions of pyrite in orogenic gold deposits show elevated Ni, As, Au, W, V and Cr (Belousov et al., 2016). In contrast, the Carlin-type deposits of Nevada tend to be associated with mildly extensional tectonics (Cline et al., 2005; Muntean et al., 2011). Mineralized lodes form in carbonate rocks enriched in carbonaceous material (Berger and Bagby, 1991; Cline et al., 2005) with ore-stage alteration consisting of decalcification, jasperoid and clay alteration (montmorillonite, kaolinite, illite and smectite), silicification and sulfidation forming at 180–240 °C and 0.5–1 kbar (Teal and Jackson, 2002; Cline et al.,

2005). Mineralization has a strong structural control which defines ore body geometries, commonly resulting in strata-bound and fault zone mineralization (Arehart, 1996). Trace element compositions of pyrite show elevated As, Au, Sb, Ti, Cu, Hg \pm Ag \pm Pb with invisible gold typically enriched in the rim zones (Large et al., 2009).

The Mount Olympus deposit shares many of the characteristics of the Carlin deposits in Nevada, although several differences are also evident (Table 6). At Mount Olympus gold mineralization is both fault-hosted and strata-bound (Morant and Doepl, 1997; Young et al., 2003). The strata-bound lodes however, occur in coarser grained rocks than those at Carlin; but similar to the Carlin deposits they have a high organic carbon content, with ore-stage alteration characterized by the removal of carbonate minerals and the addition of sericite and quartz (Wells et al., 2016). Young et al.

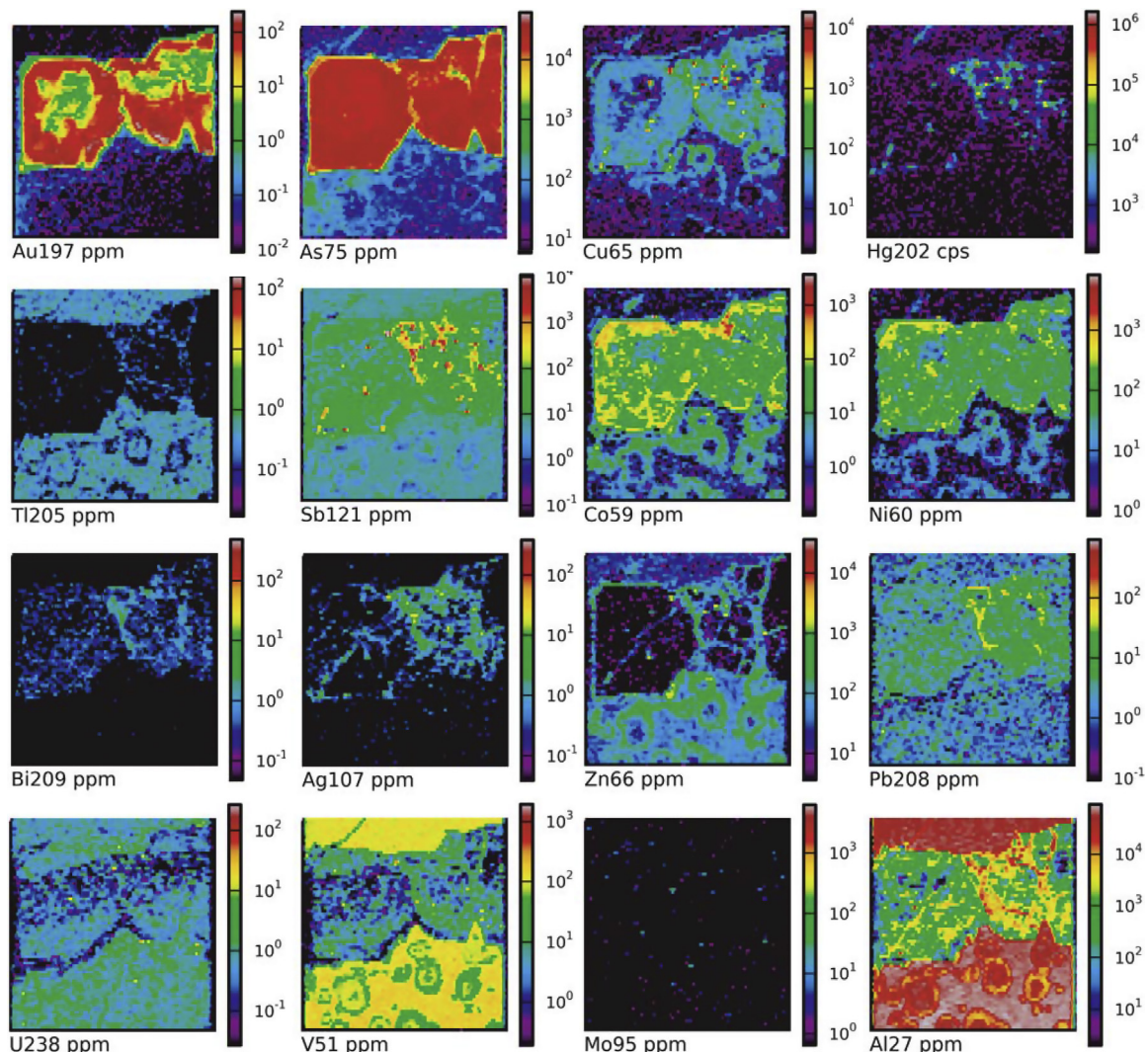


Figure 8. LA-ICP-MS images of trace elements from pyrite in MOD13 130.6 m in depth (refer to Fig. 3F) showing elevated As with a diffusive rim zone enriched in Au.

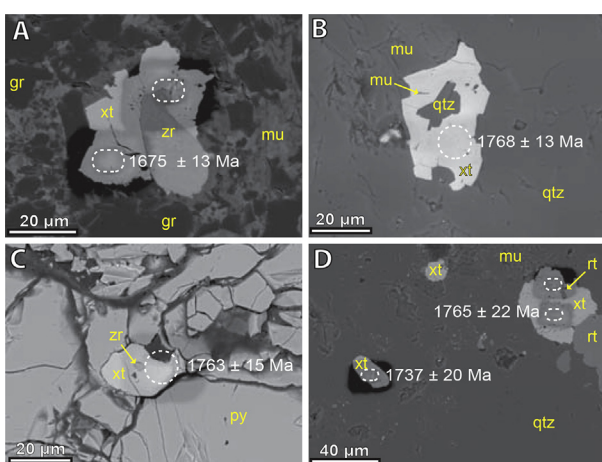


Figure 9. Scanning electron microscope-backscattered electron (SEM-BSE) images of dated xenotime crystals. White ellipses show analysis pits. Analysis pits with no ages represent discordant data. (A) Xenotime overgrowth on zircon (GSWA 219594). (B) Xenotime intergrown with muscovite and quartz from strata-bound mineralization (GSWA 909985). (C) Xenotime encased in auriferous pyrite (GSWA 209985). (D) Xenotime with inclusions of rutile (GSWA 219595). Mineral abbreviations: gr—graphite, mu—muscovite, py—pyrite, qtz—quartz, rt—rutile, xt—xenotime and zr—zircon.

(2003) indicated that the mineralization formed at temperatures and pressures up to 350 °C and 1–2 kbar, significantly higher than the Carlin deposits which formed at 180–240 °C and 0.5–1 kbar (Cline et al., 2005). However, the methods used to determine the temperature and pressure conditions at which the Mount Olympus mineralization formed are not discussed in detail, and it is difficult to assess their significance. However, since the alteration assemblages at both deposits are similar, it is possible they formed under similar conditions.

Trace element distribution maps of pyrite from Mount Olympus show geochemical similarities to the Carlin deposits of Nevada (e.g. Large et al., 2009). The relationships between Au–As, Au–Ni and Au–V for pyrites with enriched Au–As rim zones within strata-bound mineralization (MOD13), and the internal growth zones within py3 from the Zoe Fault mineralization (NMOD002) show similar compositions to the Carlin deposits. Gold forms a positive relationship with As with all data plotting below the gold saturation line defined by Reich et al. (2005) indicating that invisible gold is locked in the pyrite crystal lattice (Fig. 12A). Au–As enriched rims (MOD13), and internal bands in py3 (NMOD002) have the same composition as the hydrothermal ores of the Carlin deposits (Fig. 12A) as defined by Large et al. (2009). The rims however, are much thicker and of lower grade (up to 429 ppm Au) compared to

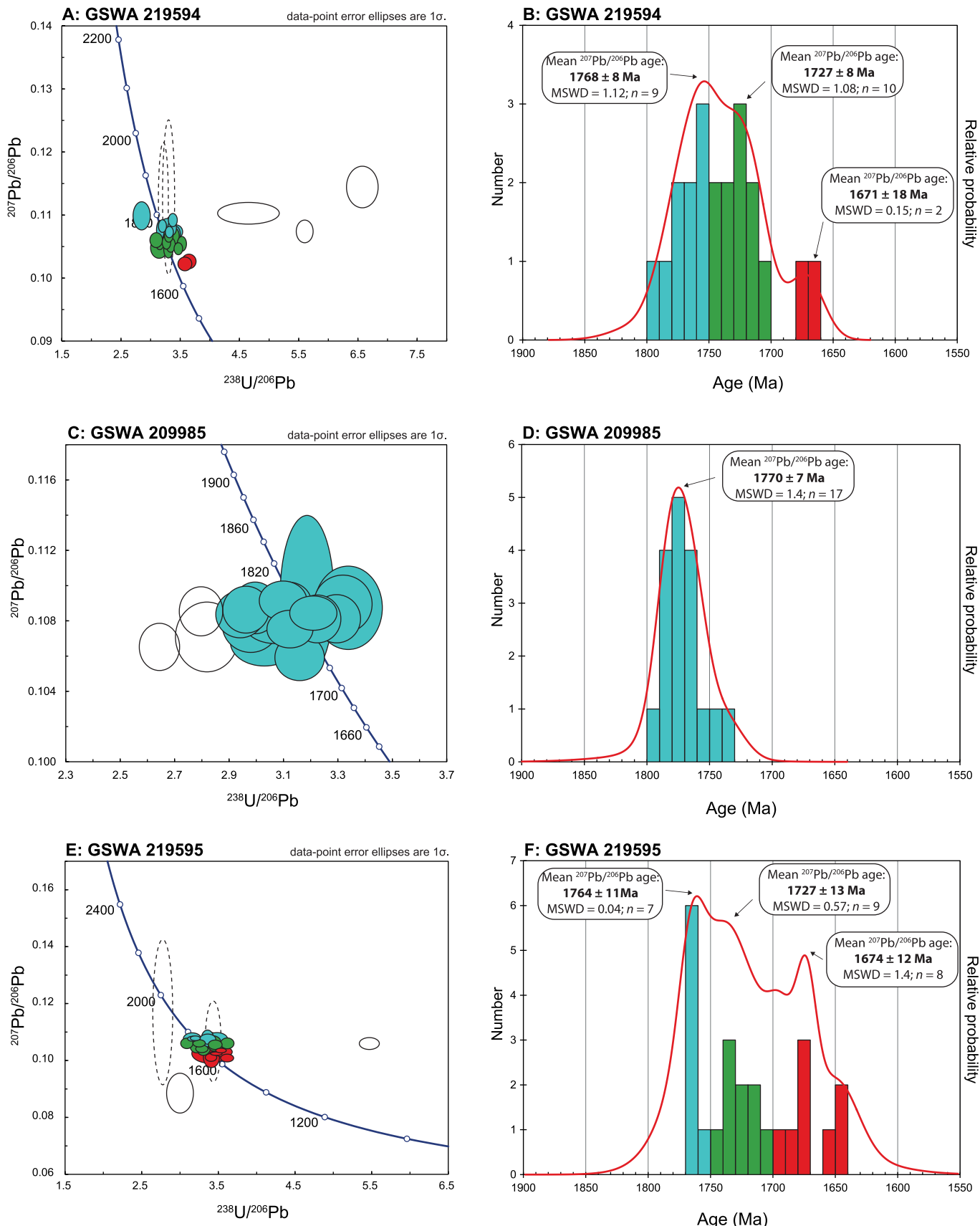


Figure 10. Tera-Wasserburg Concordia diagrams of U-Pb data for xenotime and probability density diagrams and histograms of xenotime ages for mineralized samples A and B (GSWA 219594), C and D (GSWA, 209985), E and F (GSWA 219595). Key for Concordia diagrams: colored ellipses (blue = ca. 1770 Ma, green = ca. 1730 Ma, red = ca. 1680 Ma) show data used in age calculations; other ellipses are for inferior data (unshaded black ellipses = >10% discordant data, dashed ellipses = poor spot placement). Probability density diagrams, red curve includes only data <10% discordant, colours used correspond to the Concordia diagrams.

Table 3
SHRIMP U–Pb xenotime results, GSWA 219594 Zoe Fault mineralization.

Mount No.	Grain spot	U (ppm)	Th (ppm)	Th/U	f_{206} (%)	$^{207}\text{Pb}^*/^{206}\text{Pb}^*$	$\pm 1\sigma$	$^{206}\text{Pb}^*/^{238}\text{U}$	$\pm 1\sigma$	$^{207}\text{Pb}^*/^{235}\text{U}$	$\pm 1\sigma$	$^{208}\text{Pb}^*/^{232}\text{Th}$	$\pm 1\sigma$	Disc. (%)	$^{207}\text{Pb}^*/^{206}\text{Pb}^*$ age (Ma)	$\pm 1\sigma$ (Ma)
Group 1 (1768 ± 8 Ma)																
1704	F.3-1	1747	2545	1.5	0.04	0.1100	0.0014	0.351	0.012	5.32	0.19	0.078	0.011	-8	1799	24
1704	H.1-3	1388	1318	0.9	0.01	0.1093	0.0007	0.296	0.004	4.46	0.07	0.090	0.009	6	1788	12
1704	I.1-1	1492	1275	0.9	0.05	0.1085	0.0007	0.305	0.007	4.56	0.10	0.091	0.010	3	1774	12
1705	I.1-2	1627	2152	1.3	0.16	0.1084	0.0006	0.313	0.004	4.67	0.07	0.090	0.010	1	1772	11
1704	E.1-1	1465	4320	2.9	0.04	0.1081	0.0007	0.297	0.004	4.43	0.07	0.091	0.009	5	1767	12
1704	J.2-1	1879	2508	1.3	0.07	0.1077	0.0010	0.316	0.004	4.69	0.08	0.084	0.010	0	1761	17
1704	J.1-1	1540	2490	1.6	0.12	0.1075	0.0007	0.292	0.006	4.33	0.10	0.084	0.009	6	1757	12
1704	A.1-1	2746	2849	1.0	0.01	0.1074	0.0006	0.301	0.004	4.47	0.06	0.091	0.010	3	1756	10
1704	G.1-1	2477	722	0.3	0.03	0.1071	0.0008	0.293	0.005	4.32	0.08	0.085	0.009	5	1750	14
Group 2 (1727 ± 8 Ma)																
1704	F.2-1	1915	392	0.2	0.03	0.1069	0.0007	0.302	0.004	4.45	0.07	0.058	0.010	3	1747	11
1704	H.1-1	1117	1671	1.5	0.07	0.1068	0.0008	0.294	0.005	4.32	0.08	0.089	0.010	5	1746	14
1704	K.1-1	1627	3650	2.2	0.04	0.1062	0.0008	0.323	0.007	4.73	0.11	0.096	0.010	-4	1735	14
1705	I.1-1	1053	2549	2.4	0.05	0.1061	0.0009	0.317	0.005	4.64	0.09	0.095	0.010	-2	1734	16
1705	H.3-1	2169	472	0.2	0.02	0.1058	0.0007	0.306	0.004	4.46	0.07	0.079	0.010	0	1728	12
1704	C.1-1	1550	1631	1.1	0.13	0.1056	0.0008	0.283	0.004	4.12	0.07	0.076	0.009	7	1724	13
1704	H.1-2	1144	1240	1.1	0.04	0.1054	0.0008	0.300	0.005	4.35	0.07	0.086	0.010	2	1721	13
1704	D.1-1	1808	4735	2.6	0.00	0.1049	0.0011	0.318	0.010	4.60	0.15	0.102	0.010	-4	1713	19
1704	E.2-1	2008	4459	2.2	0.07	0.1048	0.0006	0.288	0.004	4.17	0.06	0.080	0.010	5	1711	11
1705	H.1-1	1304	1171	0.9	0.14	0.1047	0.0009	0.303	0.005	4.37	0.08	0.086	0.010	0	1709	15
Group 3 (1671 ± 18 Ma)																
1704	L.1-2	1082	8441	7.8	0.01	0.1028	0.0007	0.274	0.006	3.88	0.09	0.080	0.009	7	1675	13
1704	B.1-1	1443	3309	2.3	0.05	0.1024	0.0007	0.279	0.006	3.94	0.09	0.080	0.010	5	1668	13
Discordance > 10%																
1704	L.1-1	1789	1050	0.6	0.46	0.1104	0.0014	0.215	0.016	3.27	0.24	0.075	0.007	30	1806	23
1704	G.1-2	2635	2397	0.9	0.22	0.1075	0.0011	0.178	0.003	2.65	0.05	0.069	0.006	40	1758	19
1704	E.1-2	4638	3519	0.8	0.40	0.1146	0.0020	0.152	0.004	2.40	0.08	0.054	0.005	51	1873	32
Poor spot placement																
1705	H.2-1	1374	917	0.7	0.28	0.1127	0.0056	0.311	0.005	4.83	0.27	0.074	0.009	5	1844	89
1704	F.1-1	2189	1968	0.9	0.70	0.1129	0.0076	0.303	0.006	4.71	0.35	0.087	0.009	8	1847	122

Pb* indicates radiogenic Pb.

f_{206} is the proportion of common Pb in ^{206}Pb , determined using the measured $^{204}\text{Pb}/^{206}\text{Pb}$ and a common Pb composition from the Stacey and Kramers (1975) model at the approximate age of the sample.

Disc. is apparent discordance, as $100 \times (t[^{207}\text{Pb}^*/^{206}\text{Pb}^*] - t[^{238}\text{U}/^{206}\text{Pb}^*]) / t[^{207}\text{Pb}^*/^{206}\text{Pb}^*]$.

Table 4 SHRIMP U–Pb xenotime results, GSWA 209985 strata bound mineralization – siltstone (2.67 ppm Au).

Mount No.	Grain spot	U (ppm)	Th (ppm)	Th/U	f_{206} (%)	$^{207}\text{Pb}^*/^{206}\text{Pb}^*$	$\pm 1\sigma$	$^{206}\text{Pb}^*/^{238}\text{U}$	$\pm 1\sigma$	$^{207}\text{Pb}^*/^{235}\text{U}$	$\pm 1\sigma$	$^{208}\text{Pb}^*/^{232}\text{Th}$	$\pm 1\sigma$	$^{207}\text{Pb}^*/^{206}\text{Pb}^*$ age (Ma)	$\pm 1\sigma$ (Ma)	$\pm 1\sigma$ (Ma)
Group 1 (1770 ± 7 Ma)																22
1602	10-1	4353	25774	5.9	0.10	0.1088		0.0013	0.300	0.007	4.50	0.13	0.087	0.009	5	1779
1602	3-1	2597	14060	5.4	0.28	0.1090		0.0009	0.302	0.006	4.53	0.11	0.100	0.010	5	1783
1602	9-1	2853	16426	5.8	0.00	0.1082		0.0008	0.304	0.005	4.53	0.09	0.086	0.010	3	1769
1602	17-1	2861	16796	5.9	0.55	0.1095		0.0026	0.314	0.006	4.74	0.16	0.091	0.010	2	1791
1602	13-1	3695	22984	6.2	0.03	0.1081		0.0007	0.310	0.006	4.63	0.09	0.090	0.010	1	1768
1602	15-1	2723	16850	6.2	0.04	0.1085		0.0005	0.312	0.006	4.66	0.09	0.090	0.010	1	1774
1602	1-1	2093	12552	6.0	0.10	0.1091		0.0006	0.321	0.006	4.83	0.09	0.093	0.010	-1	1784
1602	7-1	1716	9656	5.6	0.02	0.1092		0.0006	0.323	0.006	4.86	0.10	0.094	0.010	-1	1786
1602	8-1	2350	12964	5.5	0.03	0.1090		0.0006	0.325	0.008	4.88	0.12	0.094	0.010	-2	1783
1602	11-1	2121	12127	5.7	0.07	0.1076		0.0006	0.320	0.006	4.75	0.09	0.093	0.010	-2	1759
1602	16-1	1564	8925	5.7	0.10	0.1060		0.0007	0.317	0.006	4.63	0.10	0.091	0.010	-2	1731
1602	14-1	2676	15053	5.6	0.09	0.1078		0.0006	0.326	0.008	4.85	0.12	0.094	0.010	-3	1763
1602	12-1	1630	9494	5.8	0.21	0.1088		0.0008	0.334	0.006	5.01	0.10	0.098	0.010	-4	1779
1602	2-1	2098	14074	6.7	0.12	0.1068		0.0007	0.330	0.009	4.87	0.14	0.095	0.011	-5	1746
1602	6-1	1656	7402	4.5	0.05	0.1087		0.0008	0.338	0.006	5.06	0.10	0.098	0.011	-6	1777
1602	5-1	4190	21590	5.2	0.06	0.1078		0.0009	0.336	0.008	4.99	0.12	0.099	0.011	-6	1763
1602	4-1	1118	5724	5.1	0.02	0.1084		0.0008	0.340	0.007	5.09	0.11	0.097	0.011	-7	1773
Discordance >10%																13
1603	A.1-1	1603	4323	2.7	0.15	0.1086		0.0008	0.358	0.007	5.36	0.11	0.098	0.011	-11	1776
1603	E.2-1	2685	4395	1.6	0.06	0.1071		0.0012	0.355	0.010	5.25	0.16	0.102	0.011	-12	1751
1603	E.1-1	1889	2868	1.5	0.08	0.1066		0.0008	0.379	0.007	5.56	0.11	0.108	0.012	-19	1741

 Pb^* indicates radiogenic Pb.

f_{206} is the proportion of common Pb in ^{206}Pb , determined using the measured $^{204}\text{Pb}^{206}\text{Pb}$ and a common Pb composition from the Stacey and Kramers (1975) model at the approximate age of the sample.

f_{206} = the proportion of common Pb in ^{206}Pb , as $100 \times (t^{207}\text{Pb}^*/^{206}\text{Pb}^* - t^{207}\text{Pb}^*/^{206}\text{Pb}^*) / (t^{207}\text{Pb}^*/^{206}\text{Pb}^* - t^{207}\text{Pb}^*/^{206}\text{Pb}^*)$.

Disc. is apparent discordance, as $100 \times (t^{207}\text{Pb}^*/^{206}\text{Pb}^* - t^{207}\text{Pb}^*/^{206}\text{Pb}^*) / (t^{207}\text{Pb}^*/^{206}\text{Pb}^* + t^{207}\text{Pb}^*/^{206}\text{Pb}^*)$.

those in the Carlin deposits (up to 2000 ppm Au). A similar association between Au–Ni and Au–V exists with a negative relationship between Ni and V to Au for mineralized pyrite (py3 internal zone and MOD13 rims) which is comparable to the hydrothermal Carlin ores (Fig. 12B and C). Additionally, trace element distributions within py3 are identical to those at Carlin with elevated Au, As, Cu, Sb, Hg and Tl (Large et al., 2009).

Our results indicate that all of the characteristic features of the Mount Olympus deposit are significantly different from orogenic gold deposits, including those in the northern Capricorn Orogen, where mineralization is associated with the emplacement of laminated auriferous quartz–carbonate–pyrite veins, abundant native gold, and introduction of carbonate minerals during ore-stage hydrothermal alteration (Table 6; Groves et al., 1998; Fielding et al., 2017). Here we reclassify the Mount Olympus deposit as a Carlin-like deposit since it has many (but not all) characteristics in common with the Carlin-type deposits of Nevada (Table 6).

7.2. Timing of gold mineralization

Trace element mapping of pyrite from the Zoe Fault (NMOD002 py1–4) and strata-bound (MOD13) mineralization indicates that gold forms in a solid solution within Au–As-rich arsenian pyrite. Results suggest that py1 and py2 have compositions (Au–As, Au–Ni and Au–V ratios) similar to diagenetic pyrite (Fig. 12; Large et al., 2009). This is consistent with their form as crystal aggregates which occur as discontinuous layers and lenses within carbonaceous-rich layers with elevated U, V, Mo and Al content (Fig. 6). Although these pyrites are enriched in gold (mean Au py1 = 8 ppm and py2 = 2 ppm) the majority of the gold forms as diffusive Au–As-enriched rims within strata-bound mineralization (MOD13, mean Au of 55 ppm) or in Au–As-enriched internal growth zones in py3 (NMOD002; mean Au of 67 ppm) within the Zoe Fault. LA-ICP-MS images of pyrite with diffusive Au–As rims (MOD13) have comparable Au–As, Au–Ni and Au–V relationships to those of the Carlin-type ores, and to Au–As enriched internal zone of py3 which have the same geochemical element associations to Carlin-type ores (Fig. 12). Dating of hydrothermal xenotime intergrown with ore-stage alteration minerals and arsenian pyrite (Fig. 9C) within strata-bound ore from diamond drill core MOD13 yields a date of 1769 ± 5 Ma, representing the timing of hydrothermal gold mineralization.

7.3. Setting of mineralization

The Mount Olympus deposit is located on the Zoe Fault, a second order splay of the Nanjilgardy Fault, which is a crustal-scale structure (Johnson et al., 2013). The timing of gold mineralization at ca. 1770 Ma lies at the younger end of the age range for the intracratonic 1820–1770 Ma Capricorn Orogeny (Sheppard et al., 2010), a time that represents a distinct change in tectonic regime, from predominantly northeast compression to north–northwest stresses producing dextral strike-slip reactivation of the Nanjilgardy Fault (Krapež, 1999; Young et al., 2003). Furthermore, xenotime growth dated at ca. 1730 Ma (from this study and by Sener et al. (2005)) and ca. 1675 Ma is also contemporaneous with hydrothermal monazite and xenotime growth at the Paulsens gold mine located 150 km to the northwest (Fielding et al., 2017) and coincides with the early stages of the 1680–1620 Ma Manganaro Orogeny (Sheppard et al., 2005). These events are also thought to reflect the timing of punctuated reactivation on the Nanjilgardy Fault and associated hydrothermal fluid flow. These data indicate that gold mineralization at Mount Olympus occurred in an intra-cratic setting, during low- to medium-grade metamorphism and

Table 5
SHRIMP U–Pb xenotime results, GSWA 219595 strata bound mineralization – conglomerate.

Mount No.	Grain spot	U (ppm)	Th (ppm)	Th/U	f_{206} (%)	$^{207}\text{Pb}^*/^{206}\text{Pb}^*$	$\pm 1\sigma$	$^{206}\text{Pb}^*/^{238}\text{U}$	$\pm 1\sigma$	$^{207}\text{Pb}^*/^{235}\text{U}$	$\pm 1\sigma$	$^{208}\text{Pb}^*/^{232}\text{Th}$	$\pm 1\sigma$	Disc. (%)	$^{207}\text{Pb}^*/^{206}\text{Pb}^*$ age (Ma)	$\pm 1\sigma$ (Ma)
Group 1 (1764 ± 11 Ma)																
1705	G.1-1	4211	2103	0.5	0.00	0.1080	0.0006	0.312	0.004	4.65	0.07	0.091	0.010	1	1767	9
1705	D.2-4	882	1424	1.6	0.46	0.1080	0.0019	0.298	0.005	4.43	0.11	0.088	0.010	5	1765	31
1705	B.1-1	761	1038	1.4	0.00	0.1079	0.0013	0.316	0.008	4.71	0.13	0.093	0.010	0	1765	22
1705	C.3-1	4150	5350	1.3	0.00	0.1078	0.0006	0.316	0.004	4.69	0.07	0.091	0.010	0	1763	10
1705	A.3-1	514	1124	2.2	0.00	0.1078	0.0015	0.287	0.007	4.27	0.13	0.086	0.009	8	1763	25
1705	J.2-1	1284	1339	1.0	0.06	0.1078	0.0011	0.297	0.006	4.42	0.10	0.089	0.010	5	1762	19
1705	A.2-1	549	1441	2.6	0.31	0.1072	0.0019	0.295	0.008	4.36	0.14	0.088	0.010	5	1752	33
Group 2 (1727 ± 13 Ma)																
1705	C.1-1	877	1760	2.0	0.04	0.1069	0.0013	0.293	0.007	4.31	0.11	0.086	0.009	5	1748	22
1705	C.2-1	2257	2631	1.2	0.06	0.1063	0.0008	0.307	0.005	4.51	0.08	0.090	0.010	0	1737	14
1705	B.2-1	756	1145	1.5	0.37	0.1063	0.0011	0.324	0.006	4.74	0.10	0.092	0.010	-4	1737	20
1705	J.1-1	1030	1323	1.3	0.02	0.1063	0.0012	0.276	0.004	4.05	0.08	0.080	0.009	9	1737	21
1705	A.4-1	643	869	1.4	0.08	0.1058	0.0011	0.289	0.005	4.22	0.08	0.098	0.009	5	1729	18
1705	E.1-1	1112	1751	1.6	0.35	0.1055	0.0016	0.311	0.005	4.52	0.11	0.093	0.010	-1	1723	28
1705	D.2-1	754	1524	2.0	1.09	0.1053	0.0020	0.302	0.006	4.39	0.12	0.089	0.010	1	1719	36
1705	A.5-1	574	1300	2.3	0.23	0.1052	0.0011	0.289	0.005	4.19	0.09	0.083	0.010	5	1718	19
1705	C.5-1	1835	2092	1.1	0.14	0.1044	0.0009	0.304	0.005	4.38	0.08	0.086	0.010	-1	1703	15
Group 3 (1674 ± 12 Ma)																
1705	G.2-1	3961	7552	1.9	0.01	0.1038	0.0005	0.283	0.004	4.05	0.06	0.084	0.009	5	1693	10
1705	F.1-1	622	962	1.5	0.00	0.1033	0.0011	0.280	0.006	3.99	0.10	0.080	0.009	5	1685	20
1705	G.2-2	3485	6417	1.8	-0.01	0.1028	0.0005	0.288	0.004	4.09	0.06	0.084	0.010	3	1675	8
1705	A.1-1	654	1456	2.2	0.52	0.1027	0.0022	0.295	0.013	4.18	0.21	0.089	0.010	0	1674	39
1705	G.2-3	4338	7288	1.7	0.01	0.1026	0.0004	0.288	0.004	4.07	0.06	0.083	0.010	3	1672	8
1705	D.1-1	786	956	1.2	1.10	0.1014	0.0023	0.293	0.006	4.10	0.13	0.084	0.010	0	1651	42
1705	D.2-3	1104	2677	2.4	0.19	0.1014	0.0009	0.294	0.004	4.10	0.07	0.089	0.010	-1	1649	16
1705	D.2-2	724	1614	2.2	0.13	0.1011	0.0009	0.276	0.004	3.85	0.07	0.080	0.010	4	1645	16
Discordance >10%																
1705	A.1-3	805	863	1.1	1.97	0.0888	0.0044	0.333	0.013	4.08	0.26	0.084	0.013	-32	1400	95
1705	B.1-2	890	1106	1.2	0.54	0.1062	0.0013	0.183	0.003	2.68	0.05	0.075	0.006	38	1736	23
Poor spot placement																
1705	C.4-1	2645	3523	1.3	0.32	0.1172	0.0157	0.360	0.011	5.82	0.85	0.092	0.010	-4	1914	240
1705	A.1-2	816	1806	2.2	0.63	0.1070	0.0088	0.291	0.006	4.30	0.39	0.086	0.009	6	1748	151

Pb* indicates radiogenic Pb.

f_{206} is the proportion of common Pb in ^{206}Pb , determined using the measured $^{204}\text{Pb}/^{206}\text{Pb}$ and a common Pb composition from the Stacey and Kramers (1975) model at the approximate age of the sample.

Disc. is apparent discordance, as $100 \times (t[^{207}\text{Pb}^*/^{206}\text{Pb}^*] - t[^{238}\text{U}/^{206}\text{Pb}^*]) / t[^{207}\text{Pb}^*/^{206}\text{Pb}^*]$.

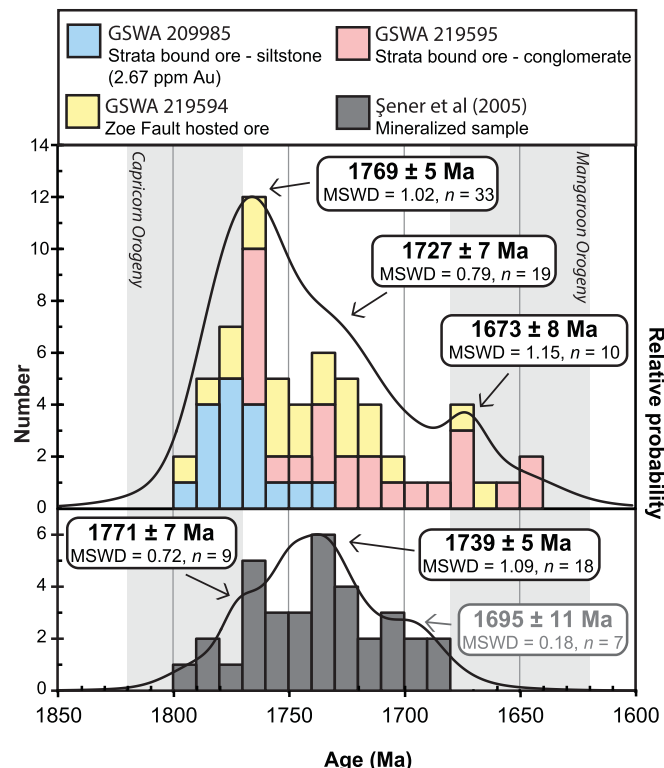


Figure 11. Probability plots and histograms with 10 Ma bin width for hydrothermal xenotime. Upper panel contains data from the strata-bound ore zone (GSWA, 209985 and 219595) and from the Zoe Fault (GSWA, 219594). The lower panel contains data from Sener et al. (2005), grey text indicates inferior data (poor spot placement or younger outliers). Weighted mean $^{207}\text{Pb}^*/^{206}\text{Pb}^*$ dates are reported with 95% confidence levels including data <10% discordant that contain $\leq 1\%$ common Pb.

was facilitated by the focusing of hydrothermal fluids along a major crustal structure.

7.4. Regional-scale drivers to mineral systems

Despite the notion that orogenic, epithermal and Carlin-type gold deposits may represent a continuum of deposit types (Huston et al., 2016), with their individual characteristics defined

principally by processes operating at the smallest-scales of the mineral system (Nesbitt, 1988; Robert et al., 2007; Dill, 2010; Brauhart et al., 2017), the data presented here demonstrate that there are distinct large-scale drivers for the three deposit types. Whereas orogenic gold deposits are driven by high-energy, plate margin processes associated with accretionary or collisional tectonics (Groves et al., 1998; Goldfarb et al., 2001), and epithermal deposits are driven by regional-scale magmatic processes (e.g. Simmons et al., 2005), Carlin-type deposits may form in a variety of settings (Hu et al., 2002; Cline et al., 2005; Muntean et al., 2011), provided there is an appropriate energy source (orogeny or magmatism) and favorable architecture (crustal-scale faults). The juxtaposition of tectonic blocks during collisional and accretionary orogenesis commonly results in the generation of orogenic belts that contain numerous crustal-scale structures and suture zones (Cook and Erdmer, 2005; Johnson et al., 2013). Since these belts are particularly susceptible to reactivation, they may not only contain orogenic gold deposits associated with the original collisional/accretion phase (Fielding et al., 2017), but also overprinting Carlin-like gold events. Without precise geochronology it is not possible to unravel the difference in timing and setting of these deposits, particularly in areas where the deposits have been overprinted by subsequent hydrothermal or mineralizing events.

8. Conclusions

Although previous researchers noted similarities between the Mount Olympus deposit and the Carlin-type deposits of Nevada (Young et al., 2003), Mount Olympus was classified as an orogenic gold deposit, largely due to the interpretation that xenotime growth at ca. 1738 Ma was related to the assembly of Proterozoic Australia (Sener et al., 2005). At a regional scale, the deposit does not share the characteristics of an orogenic deposit, as it formed during the waning stages of the intracratonic 1820–1770 Ma Capricorn Orogeny far from any active continental margin, and after the cessation of all felsic magmatism associated with this event (Sheppard et al., 2010). The data presented here uphold the division in hydrothermal gold types (oreogenic, epithermal and Carlin) indicating that, at a mineral system level, the regional-scale drivers for each are different. Although many gold deposits worldwide are associated with collisional or accretionary orogenesis (Goldfarb et al., 2001), substantial gold deposits such as Carlin-like gold deposits can form in an intracratonic setting during regional-scale crustal reworking.

Table 6
Comparison between Orogenic, Carlin-type and Mount Olympus ores.

	Orogenic	Carlin-type	Mount Olympus
Temperature and pressure	200–650 °C, 0.5–5 kbar	180–240 °C, 0.5–1 kbar	<350 °C 1–2 kbar
Major host rocks	Greenstones and turbidites	Shelf carbonate with high carbon content	Deltaic deposits and shelf carbonated with high carbon content
Alteration	Sericite, quartz, carbonate	Illitic sericite, quartz, jasperoid, removal of carbonate	Illitic sericite, quartz, removal of carbonate
Gold form	Abundant free gold; minor solid solution in pyrite	Solid solution in pyrite	Solid solution in pyrite; rare free gold in cracks and fractures
Trace element associations	Au, Ag, As, Te, Sb, W, S	Au, As, Sb, Cu, Ti, Hg	Au, As, Cu, Sb, Hg, Ti
Quartz veining	Abundant	Absent	Rare; within the Zoe Fault
Gold setting	Dominantly quartz veins	Areas of increased porosity and permeability (faults, hinge zones of anticlines, lithological contacts, etc.)	Areas of increased porosity and permeability (e.g. Zoe Fault, porous conglomerate and sandstone)
Tectonic setting	Compressional	Mildly extensional	Strike slip transpressional, compressional?
Age of mineralization	>3.0 Ga, ca. 2.8–2.55 Ga, ca. 2.1 –1.8 Ga	42–36 Ma	ca. 1.7 Ga

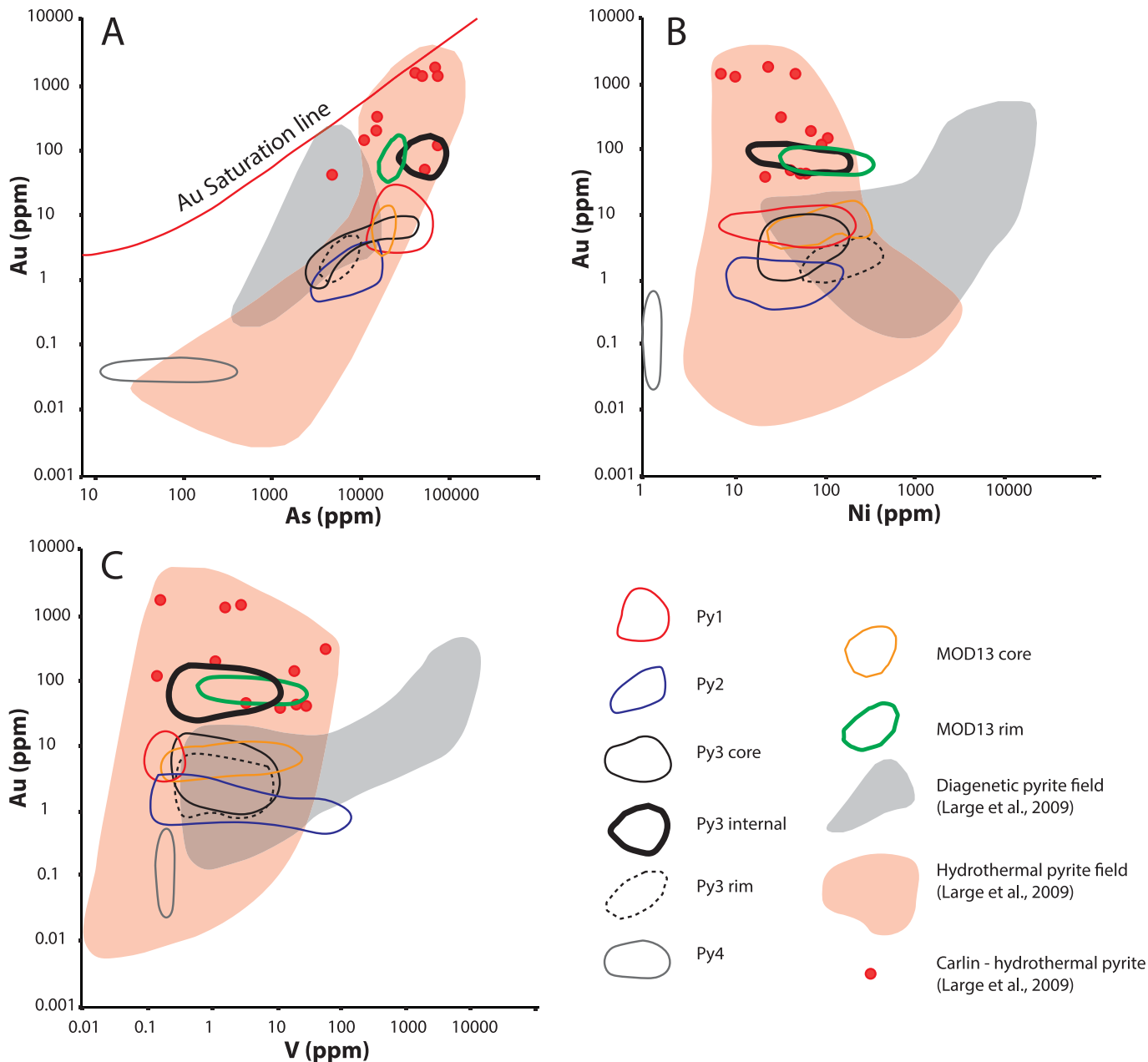


Figure 12. Binary plots showing comparisons of trace element concentrations in pyrite between Carlin (Large et al., 2009) and Mount Olympus mineralization. (A) Au–As; (B) Au–Ni and (C) Au–V.

Acknowledgments

This project was funded through an ARC linkage grant (LP130100922) and industry scholarship by Northern Star Resources as a part of a PhD by I. O. H. Fielding. S. P. Johnson publishes with the permission of the director of the Geological Survey of Western Australia. Xenotime and baddeleyite analyses were carried out on the Sensitive High Resolution Ion Micro Probe mass spectrometer (SHRIMP II) at the John de Laeter Centre, Curtin University, with the financial support of the Australian Research Council and Auscope NCRIS. Pyrite trace element maps and images were analyzed by researchers at CODES, University of Tasmania and were funded through AMIRA P1041 sponsored by AngloGold Ashanti Limited, G-Resources Group, Issara Mining Limited, Newcrest

Mining Limited, Newmont USA Limited, Northern Star Resources Ltd, Sipa Resources Limited. We thank an anonymous reviewer for the helpful comments.

References

- Arehart, G.B., 1996. Characteristics and origin of sediment-hosted disseminated gold deposits: a review. *Ore Geology Reviews* 11 (6), 383–403.
- Berger, B.R., Bagby, W.C., 1991. *The Geology and Origin of Carlin-type Gold Deposits, Gold Metallogeny and Exploration*. Springer US, Boston, MA, pp. 210–248.
- Belousov, I., Large, R.R., Meffre, S., Danyushevsky, L.V., Steadman, J., Beardmore, T., 2016. Pyrite compositions from VHMS and orogenic Au deposits in the Yilgarn Craton, Western Australia: implications for gold and copper exploration. *Ore Geology Reviews* 79, 474–499.

- Brauhart, C.W., Grunsky, E.C., Hagemann, S.G., 2017. Magmato-hydrothermal space: a new metric for geochemical characterisation of metallic ore deposits. *Ore Geology Reviews* 86, 867–895.
- Cline, J.S., Hofstra, A.H., Muntean, J.L., Tosdal, R.M., Hickey, K.A., 2005. Carlin-type gold deposits in Nevada: critical geologic characteristics and viable models. *Economic Geology 100th Anniversary Volume* 451–484.
- Cook, F., Erdmer, P., 2005. An 1800 km cross section of the lithosphere through the northwestern North American plate: lessons from 4.0 billion years of Earth's history. *Canadian Journal of Earth Sciences* 42 (6), 1295–1311.
- Danyushevsky, L., Robinson, P., Gilbert, S., Norman, M., Large, R., McGoldrick, P., Shelley, M., 2011. Routine quantitative multi-element analysis of sulphide minerals by laser ablation ICP-MS: standard development and consideration of matrix effects. *Geochemistry Exploration Environment Analysis* 11 (1), 51–60.
- Dill, H.G., 2010. The "chessboard" classification scheme of mineral deposits: mineralogy and geology from aluminum to zirconium. *Earth Science Reviews* 100 (1), 1–420.
- Fielding, I.O.H., Johnson, S.P., Zi, J.-W., Rasmussen, B., Muhling, J.R., Dunkley, D.J., Sheppard, S., Wingate, M.T.D., Rogers, J.R., 2017. Using *in situ* SHRIMP U-Pb monazite and xenotime geochronology to determine the age of orogenic gold mineralization: an example from the Pausens mine. *Southern Pilbara Craton Economic Geology* 112 (5), 1205–1230.
- Fletcher, I.R., McNaughton, N.J., Aleinikoff, J.A., Rasmussen, B., Kamo, S.L., 2004. Improved calibration procedures and new standards for U–Pb and Th–Pb dating of Phanerozoic xenotime by ion microprobe. *Chemical Geology* 209 (3–4), 295–314.
- Fletcher, I.R., Rasmussen, B., McNaughton, N.J., 2000. SHRIMP U–Pb geochronology of authigenic xenotime and its potential for dating sedimentary basins. *Australian Journal of Earth Sciences* 47 (5), 845–859.
- Goldfarb, R.J., Groves, D.I., 2015. Orogenic gold: common or evolving fluid and metal sources through time. *Lithos* 233, 2–26.
- Goldfarb, R.J., Groves, D.I., Gardoll, S., 2001. Orogenic gold and geologic time: a global synthesis. *Ore Geology Reviews* 18 (1–2), 1–75.
- Groves, D.I., Goldfarb, R.J., Gebre-Mariam, M., Hagemann, S.G., Robert, F., 1998. Orogenic gold deposits: a proposed classification in the context of their crustal distribution and relationship to other gold deposit types. *Ore Geology Reviews* 13 (1–5), 7–27.
- Groves, D.I., Goldfarb, R.J., Robert, F., Hart, C.J.R., 2003. Gold deposits in metamorphic belts: overview of current understanding, outstanding problems. *Future Research and Exploration Significance Economic Geology* 98 (1), 1–29.
- Hronsky, J.M., Groves, D.I., Loucks, R.R., Begg, G.C., 2012. A unified model for gold mineralisation in accretionary orogens and implications for regional-scale exploration targeting methods. *Mineralium Deposita* 47 (4), 339–358.
- Hu, R.-Z., Su, W.-C., Bi, X.-W., Tu, G.-Z., Hofstra, A.H., 2002. Geology and geochemistry of Carlin-type gold deposits in China. *Mineralium Deposita* 37, 378–392.
- Huston, D.L., Mernagh, T.P., Hagemann, S.G., Doublier, M.P., Fiorentini, M., Champion, D.C., Lynton Jaques, A., Czarnota, K., Cayley, R., Skirrow, R., Bastrakov, E., 2016. Tectono-metallogenic systems — the place of mineral systems within tectonic evolution, with an emphasis on Australian examples. *Ore Geology Reviews* 76, 168–210.
- Johnson, S.P., Korhonen, F.J., Kirkland, C.L., Cliff, J.B., Belousova, E.A., Sheppard, S., 2017. An isotopic perspective on growth and differentiation of Proterozoic orogenic crust: from subduction magmatism to cratonization. *Lithos* 268–271, 76–86.
- Johnson, S.P., Sheppard, S., Rasmussen, B., Wingate, M.T.D., Kirkland, C.L., Muhling, J.R., Fletcher, I.R., Belousova, E.A., 2011. Two collisions, two sutures: punctuated pre-1950 Ma assembly of the West Australian craton during the ophthalmian and Glenburgh orogenies. *Precambrian Research* 189 (3–4), 239–262.
- Johnson, S.P., Thorne, A.M., Tyler, I.M., Korsch, R.J., Kennett, B.L.N., Cutten, H.N., Goodwin, J., Blay, O., Blewett, R.S., Joly, A., Dentith, M.C., Aitken, A.R.A., Holzschuh, J., Salmon, M., Reading, A., Heinson, G., Boren, G., Ross, J., Costeloe, R.D., Fomin, T., 2013. Crustal architecture of the Capricorn orogen, Western Australia and associated metallogeny. *Australian Journal of Earth Sciences* 60 (6–7), 681–705.
- Korhonen, F.J., Johnson, S.P., Wingate, M.T.D., Kirkland, C.L., Fletcher, I.R., Dunkley, D.J., Roberts, M.P., Sheppard, S., Muhling, J.R., Rasmussen, B., 2017. Radiogenic heating and craton-margin plate stresses as drivers for intraplate orogeny. *Journal of Metamorphic Geology* 35, 631–661.
- Krapež, B., 1999. Stratigraphic record of an Atlantic-type global tectonic cycle in the palaeoproterozoic Ashburton province of Western Australia. *Australian Journal of Earth Sciences* 46 (1), 71–87.
- Krapež, B., Müller, S.G., Bekker, A., 2015. Stratigraphy of the late palaeoproterozoic (~2.03 Ga) Wooly dolomite, Ashburton province, Western Australia: a carbonate platform developed in a failed rift basin. *Precambrian Research* 271, 1–19.
- Large, R.R., Danyushevsky, L., Hollit, C., Maslennikov, V., Meffre, S., Gilbert, S., Bull, S., Scott, R., Emsbo, P., Thomas, H., Singh, B., Foster, J., 2009. Gold and trace element zonation in pyrite using a laser imaging technique: implications for the timing of gold in orogenic and carlin-style sediment-hosted deposits. *Economic Geology* 104 (5), 635–668.
- Ludwig, K.R., 2003. Isoplot/Ex Version 3.00, a Geochronological Toolkit for Microsoft Excel, vol. 4. Berkeley Geochronology Centre Special Publication, p. 73.
- Ludwig, K.R., 2009. Squid 2.50, a User's Manual. Berkeley Geochronology Centre, Berkeley, California, USA, p. 95.
- McCuag, T.C., Hronsky, J.M.A., 2014. The mineral systems concept: the key to exploration targeting. In: Kelly, K.D., Golden, H.C. (Eds.), *Building Exploration Capability for the 21st Century*, vol. 18. Society of Economic Geologists: Special Publication, pp. 153–175.
- Morant, P., Doepel, G., 1997. The Mount Olympus Gold Deposit: New Generation Gold Mines, vol. 97. Australian Mineral Foundation, Perth, Western Australia, pp. 6.1–6.9.
- Muntean, J.L., Cline, J.S., Simon, A.C., Longo, A.A., 2011. Magmatic-hydrothermal origin of Nevada's Carlin-type gold deposits. *Nature Geoscience* 4 (2), 122–127.
- Nesbitt, B.E., 1988. Gold deposit continuum: a genetic model for lode Au mineralization in the continental crust. *Geology* 16 (11), 1044–1048.
- Northern Star Resources Limited, 2015. Northern Star Resources Limited 2015 Annual Report. <http://www.nsrltd.com/wp-content/uploads/2015/08/NST-Annual-Report-2015-26-8-2015-new-cover1.pdf>.
- Rasmussen, B., Sheppard, S., Fletcher, I.R., 2006. Testing ore deposit models using *in situ* U-Pb geochronology of hydrothermal monazite: Paleoproterozoic gold mineralization in northern Australia. *Geology* 34 (2), 77–80.
- Reich, M., Kesler, S.E., Utsunomiya, S., Palenik, C.S., Chryssoulis, S.L., Ewing, R.C., 2005. Solubility of gold in arsenian pyrite. *Geochimica et Cosmochimica Acta* 69 (11), 2781–2796.
- Robert, F., Brommecker, R., Bourne, B.T., Dobak, P.J., McEwan, C.J., Rowe, R.R., Azhou, X., 2007. Models and Exploration Methods for Major Gold Deposit Types in Milkereit, B. In: *Exploration 07*, Fifth Decennial International Conference on Mineral Exploration, Toronto, Canada. Decennial Mineral Exploration Conferences, pp. 691–711.
- Sener, A.K., Young, C., Groves, D.I., Krapež, B., Fletcher, I.R., 2005. Major orogenic gold episode associated with Cordilleran-style tectonics related to the assembly of Paleoproterozoic Australia? *Geology* 33, 225–228.
- Sheppard, S., Rasmussen, B., Muhling, J.R., Farrell, T.R., Fletcher, I.R., 2007. Grenvillian-aged orogenesis in the palaeoproterozoic Gascoyne complex, Western Australia: 1030–950 Ma reworking of the proterozoic Capricorn orogen. *Journal of Metamorphic Geology* 25, 477–494.
- Sheppard, S., Occhipinti, S.A., Nelson, D.R., 2005. Intracontinental reworking in the Capricorn orogen, Western Australia: the 1680–1620 Ma Mangaroon orogeny. *Australian Journal of Earth Sciences* 52, 443–460.
- Sheppard, S., Bodorkos, S., Johnson, S.P., Wingate, M.T.D., Kirkland, C.L., 2010. The Paleoproterozoic Capricorn Orogeny: intracontinental reworking not continent–continent collision. *Geological Survey of Western Australia Report* 108, 33.
- Simmons, S.F., White, N.C., John, D.A., 2005. Geological characteristics of epithermal precious and base metal deposits. In: Hedenquist, J.W., Thompson, J.F.H., Goldfarb, R.J., Richards, J.P. (Eds.), *Economic Geology 100th Anniversary Volume*. Society of Economic Geologists, pp. 485–522.
- Stacey, J.S., Kramers, J.D., 1975. Approximation of terrestrial lead isotope evolution by a two-stage model. *Earth and Planetary Science Letters* 26, 207–221.
- Stern, R.A., Rayner, N., 2003. Ages of Several Xenotime Megacrysts by ID-TIMS: Potential Reference Materials for Ion Microprobe U-Pb Geochronology: Radioactive Age and Isotopic Studies: Report 16. Geological Survey of Canada: Current Research 2003-F1, p. 7.
- Teal, L., Jackson, M., 2002. Geologic overview of the Carlin trend gold deposits: gold deposits of the Carlin trend. *Nevada Bureau of Mines and Geology, Bulletin* 111, 9–19.
- Thorne, A.M., Seymour, D.B., 1991. Geology of the Ashburton basin Western Australia. *Geological Survey of Western Australia Bulletin* 139, 162.
- Tyler, I.M., Thorne, A.M., 1990. The northern margin of the Capricorn Orogen, Western Australia—an example of an Early Proterozoic collision zone. *Journal of Structural Geology* 12, 685–701.
- Wells, M., Laukamp, C., Hancock, E.A., 2016. Reflectance spectroscopic characterisation of mineral alteration footprints associated with sediment-hosted gold mineralisation at Mt Olympus (Ashburton Basin, Western Australia). *Australian Journal of Earth Sciences* 63, 987–1002.
- Wyborn, L.A.I., Heinrich, C.A., Jaques, A.L., 1994. Australian Proterozoic mineral systems: essential ingredients and mappable criteria. In: Hallenstein, P.C. (Ed.), *Australian Mining Looks North — the Challenges and Choices*. Australian Institute of Mining and Metallurgy; 1994 AUSIMM Annual Conference, Darwin, Northern Territory, pp. 109–115.
- Young, C.J., Groves, D.I., Morant, P., 2003. Sediment-hosted disseminated gold mineralisation in the Palaeoproterozoic Ashburton Province, Western Australia: a new epizonal orogenic gold province related to Capricorn Orogeny? In: Eliopoulos, et al. (Eds.), *Mineral exploration and Sustainable Development, Proceedings of the 7th Biennial SGA Meeting*. Millpress, Athens, Greece, pp. 835–838.